2024-05-14

Assessing the geometry of the Main Himalayan thrust in central Nepal: A thermokinematic approach

Ghoshal, S

10.1130/ges02731.1
Geosphere
Geological Society of America

Research Paper

GEOSPHERE

GEOSPHERE

https://doi.org/10.1130/GES02731.1

9 figures; 3 tables; 1 set of supplemental files

CORRESPONDENCE:
suryodoy.ghoshal@plymouth.ac.uk

CITATION: Ghoshal, S., McQuarrie, N., Robinson, D.M., and Ehlers, T.A., 2024, Assessing the geometry of the Main Himalayan thrust in central Nepal: A thermokinematic approach: Geosphere, https://doi.org/10.1130/GES02731.1.

Science Editor: David E. Fastovsky
Associate Editor: Gregory D. Hoke

Received 2 November 2023
Revision received 26 March 2024
Accepted 14 April 2024

Published online 14 May 2024

Assessing the geometry of the Main Himalayan thrust in central Nepal: A thermokinematic approach

S. Ghoshal[1,2], N. McQuarrie[1], D.M. Robinson[3], and T.A. Ehlers[4]

[1]Department of Geology and Environmental Science, University of Pittsburgh, Pittsburgh, Pennsylvania 15260-3332, USA
[2]School of Geography, Earth and Environmental Sciences, University of Plymouth, Plymouth PL4 8AA, UK
[3]Department of Geological Sciences and Center for Sedimentary Basin Studies, University of Alabama, Tuscaloosa, Alabama 35487-0338, USA
[4]School of Geographical and Earth Sciences, University of Glasgow, Glasgow G12 8QQ, UK

ABSTRACT

Since the 2015 Gorkha earthquake in Nepal, the relationship between the geometry of megathrusts and the control it exerts over the nucleation and propagation of major earthquakes has become an important topic of debate. In this study, we integrate new geologic mapping, a newly interpreted cross section from the Daraundi valley of central Nepal, two published cross sections from the neighboring Marsyangdi and Budhi Gandaki valleys, and a suite of 270 thermochronometric ages to create an integrated and validated three-dimensional kinematic model for the central Nepal Himalaya. We use this model to investigate the assertion that the westward propagation of the Gorkha rupture was restricted by deep-seated structures in the Main Himalayan thrust. The integrated kinematic model based on these cross sections indicates that the ~30 km southward step in the Main Central thrust system mapped in the Daraundi valley, along with the corresponding step in the distribution of reset muscovite (Ar-Ar) ages, is not the result of a lateral structure in the modern Main Himalayan thrust. Instead, the step in the surface geology is the result of a considerably shorter Trishuli thrust sheet in the Daraundi transect (~30 km compared to between 105 and 120 km in the other transects). The corresponding southward step in the distribution of reset muscovite Ar-Ar ages is the result of the Lesser Himalayan duplex being completely translated over the Main Himalayan thrust ramp, elevating and exposing rocks heated to >400 °C farther south in the Daraundi transect. Our integrated model also highlights the 10–15 km of out-of-sequence thrusting that occurs on the Main Central thrust system across central Nepal. Importantly, these out-of-sequence thrusts sole directly into the modern Main Himalayan thrust ramp, and, together with the distribution of reset zircon (U-Th)/He and apatite fission track ages, show that the modern ramp is distinctly linear from east to west, with no support for a lateral structure at the ramp or to the south.

1. INTRODUCTION

In 2015, the M_w 7.8 Gorkha earthquake occurred on the Main Himalayan thrust (MHT) in central Nepal (Avouac et al., 2015; USGS, 2015; Yagi and Okuwaki, 2015), the primary décollement accommodating the convergence between India and Asia at ~20 mm yr^{-1} (Bilham et al., 1997; Lavé and Avouac, 2000; Jouanne et al., 2004; Bettinelli et al., 2006; Ader et al., 2012). Geodetic and seismic studies of the MHT prior to the earthquake suggest that it was uniformly locked along its length (Ader et al., 2012; Stevens and Avouac, 2015), implying that any ruptures occurring on it should be able to easily propagate in any direction. However, the Gorkha rupture was limited to a 150-km-long, ~50-km-wide segment of the MHT, propagating exclusively eastwards from its epicenter (Avouac et al., 2015; Grandin et al., 2015). Notably, this segment is located within the zone affected by the 1833 earthquake (M_w 7.3) and appears to share its western extent (Mugnier et al., 2013, 2017). This raises the question: Is there a change in the geometry of the MHT that inhibited the propagation of these ruptures toward the west? Because the magnitude of energy released by an earthquake is directly proportional to the area of the rupture (Scholz, 1998), the locations of such barriers to the propagation of ruptures and the isolated zones of slip that they delineate can provide insight into the amount of energy that can potentially be released in future Himalayan earthquakes.

Following the Gorkha earthquake, models for the geometry of the MHT were proposed as mechanisms to explain the eastern and western boundaries of the rupture (Hubbard et al., 2016; Mugnier et al., 2017). Mugnier et al. (2017) suggested that the boundaries are the result of lateral ramps in the MHT, formed due to offsets in the pre-Himalayan basement that lowered the depth of the décollement in the rupture region. These proposed deep-seated structures were thought to be expressed at the surface as lineaments formed by aligned offsets of lithologic boundaries and topographic features, e.g., the Judi and Gaurishankar lineaments (Kayal, 2008; Mugnier et al., 2011) (Fig. 1). Hubbard et al. (2016) suggested that the ruptured MHT surface in central Nepal is contained between two ramps that are separated by 50 km in the center of the ruptured patch and merge together toward both the eastern extent of the rupture and toward the Gorkha epicenter in the west (Hubbard et al., 2016; Qiu et al., 2016). Although the details of how the MHT is compartmentalized are different, both of these models suggest that the extent of the Gorkha rupture, as well as the propagation extent of historical earthquakes, was controlled by the locations of ramps in the MHT (Hubbard et al., 2016; Mugnier et al., 2017). Ramps in the décollement control the location and magnitude of uplift and associated erosional exhumation of rocks, exerting a first-order control on

Nadine McQuarrie https://orcid.org/0000-0001-6529-778X

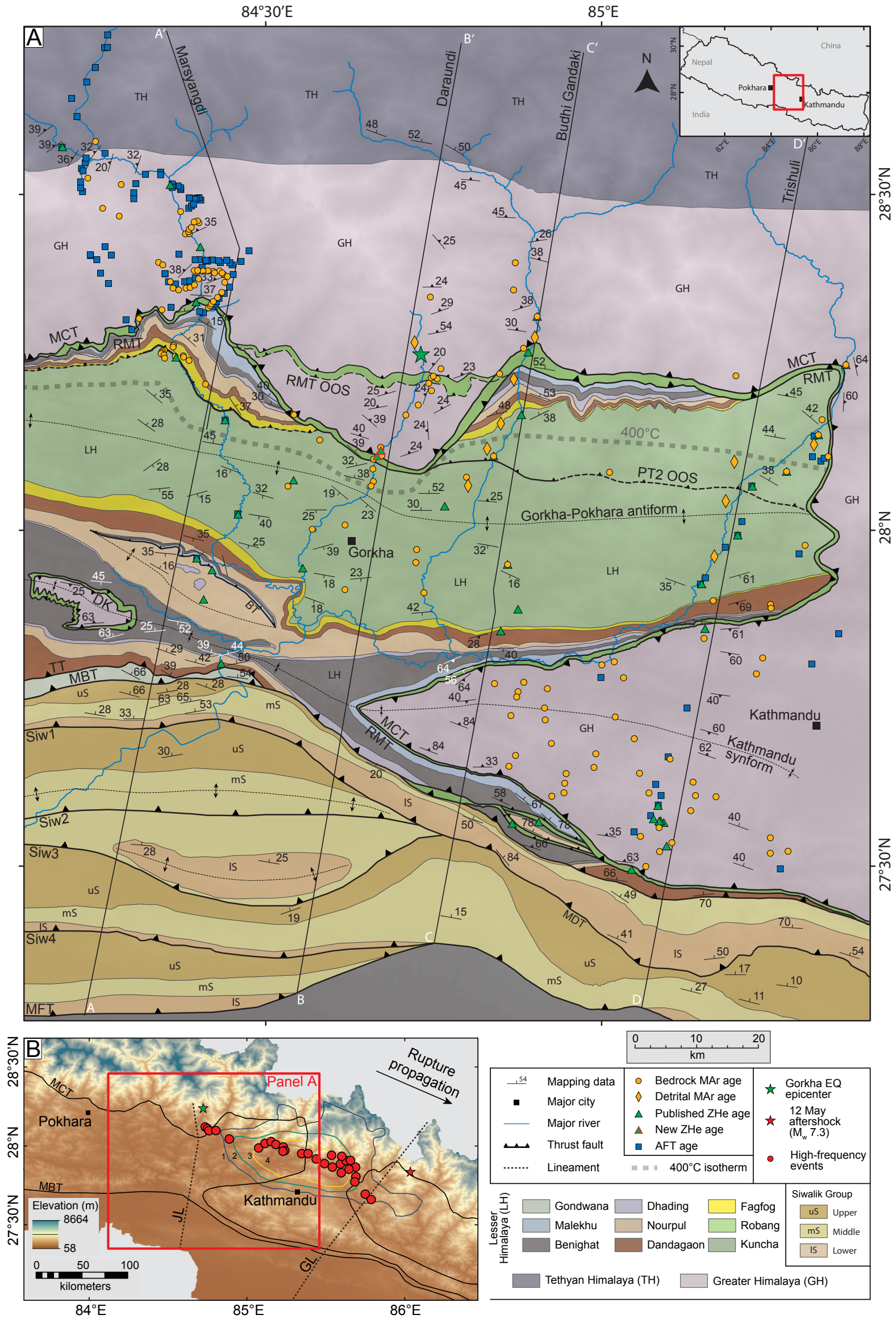

Figure 1. (A) Geologic map of central Nepal, showing the distribution of measured muscovite Ar-Ar (MAr), zircon (U-Th)/He (ZHe), and apatite fission track (AFT) thermochronological ages. Geology shown is based on new mapping in the region, combined with past mapping from Kimura (1999), Cross (2014), Khanal (2014), Dhital (2015), Lavé and Avouac (2000), Pearson (2002), Khanal and Robinson (2013), Olree (2018), and Larson et al. (2010). Rocks to the north of the gray dashed line have been heated above 400 °C. Out-of-sequence (OOS) faults are shown at physiographic transition 2 (PT2) (Wobus et al., 2003, 2006; Hodges et al., 2004; Whipple et al., 2016) and at the base of the Ramgarh-Munsiari thrust (RMT) (Hodges et al., 2004; Ghoshal et al., 2023). MCT—Main Central thrust; BT—backthrust; TT—Trishuli thrust; MBT—Main Boundary thrust; Siw1–Siw4—intra–Siwalik Group thrusts; MDT—Main Dun thrust; MFT— Main Frontal thrust; DK—Damauli klippe. (B) Regional elevation map with the complete rupture length of the 2015 Gorkha earthquake (EQ) delineated by red circles moving from west to east (Avouac et al., 2015) (propagation direction indicated by black arrow), relative to a generalized surface trace of the MCT. Slip distance (m) is shown in colored contours (Avouac et al., 2015). Gorkha epicenter is marked by a green star, while the major M_w 7.3 aftershock is indicated by a red star. JL—Judi lineament; GL—Gaurishankar lineament (Mugnier et al., 2017). Red box shows the extent shown in A.

measured thermochronometers at the surface (Shi and Wang, 1987; Ruppel and Hodges, 1994; Rahn and Grasemann, 1999; Huntington et al., 2007; Lock and Willett, 2008; Robert et al., 2011; McQuarrie and Ehlers, 2017). Because measured thermochronological cooling ages are the result of the cumulative thermal history of rocks, from their burial to exhumation at the surface, the distribution of cooling ages at the surface can be used to identify marked changes in the MHT geometry or depth across the western boundary of the Gorkha rupture extent.

The existence of a pronounced lateral boundary to the west of the Gorkha epicenter is supported by both an offset in the surface trace of the Main Central thrust (MCT) as well as an offset in the distribution of young (<5 Ma) muscovite $^{40}Ar/^{39}Ar$ (MAr) ages (Figs. 1 and 2). New mapping in the Daraundi valley, proximal to the proposed Judi lineament (Kayal, 2008; Mugnier et al., 2017), shows that the traces of the MCT and Ramgarh-Munsiari thrust step ~30 km southwards from their locations to the east (Budhi Gandaki valley) (Fig. 1). Intriguingly, there is a marked southward step in the distribution of young MAr ages, closely following the mapped expression of the MCT (Fig. 2). In contrast, zircon (U-Th)/He (ZHe) and apatite fission track (AFT) ages show a much more linear distribution across central Nepal (Figs. S1A and S1B in the Supplemental Material[1]). There are two main ways in which these offset features may have formed: (1) a lateral ramp in the modern MHT (e.g., Hubbard et al., 2016; Mugnier et al., 2017) or (2) a change in the cumulative history of uplift and exhumation experienced by the rocks being translated over the MHT. For the first of these options to be true, we would expect the modern MHT ramp to exhibit a southward offset similar to those observed in the surface geology and the distribution of MAr ages. This offset in the ramp of the MHT would allow the Greater Himalayan sequence to be exposed farther to the south and advect cooling ages toward the south. The second option requires that the differences in mapped lithology and cooling ages observed at the surface are the result of one or more changes in the MHT geometry in the past and the resulting thermal history of the rocks it carries. Lateral changes in the geometry of deformation and exhumation in the past do not require any lateral variations in the geometry of the modern MHT to explain the southward step in the Greater Himalayan rocks or the young MAr cooling ages.

In this paper, we use the relationship between the location of ramps and cooling ages to assess the modern geometry of the Main Himalayan thrust in central Nepal to test two hypotheses: (1) The MHT changes laterally from east to west, or (2) the changes that we see at the surface are due to changes in the geometry of the MHT in the past. We present a new balanced cross section and detailed kinematic model through the Daraundi valley of central Nepal, intersecting the southward step in the surface trace of the MCT. We combine this new section with cross sections from the Marsyangdi and Budhi Gandaki valleys (Ghoshal et al., 2020, 2023) to assess the geometry of the modern MHT across the western portion of the Gorkha earthquake rupture. Combining the sequential kinematics from each of these three sections with a thermokinematic model (Pecube-D; Ehlers, 2023) allows us to reproduce the exhumation and cooling histories of the rocks exposed at the surface and predict the resulting cooling ages. We constrain the models by comparing these predicted cooling ages to measured ones from the region, allowing us to invalidate and discard models that do not reproduce the distribution of cooling ages. This approach allows us to (1) disentangle the effects of changes in the modern décollement from the effects of changes in the upper-plate history on the surface geology and thermochronology and (2) highlight which of these changes are required to match the pronounced lateral variations at the surface.

2. GEOLOGIC SETTING OF THE DARAUNDI VALLEY

2.1 Subhimalaya

The Subhimalaya are made up of foreland basin sediments eroded from the rising Himalaya in the north, deposited and lithified into the Siwalik Group (Gansser, 1964; Tokuoka et al., 1986; Harrison et al., 1993; Quade et al., 1995; Burbank et al., 1996; DeCelles et al., 1998; Gautam and Rösler, 1999; Ojha et al., 2000, 2009). The Siwalik Group coarsens upwards from siltstone and mudstone at the bottom to sandstone and conglomerate at the top and is informally divided into three members, the lower, middle, and upper (Tokuoka et al., 1986; Harrison et al., 1993; Quade et al., 1995; Ojha et al., 2009). In central Nepal, all three members are exposed at the surface with a total measured thickness of ~5 km (Tokuoka et al., 1986; Harrison et al., 1993) (Fig. 1). In the south, the Siwalik Group is bound by the Main Frontal thrust (MFT), which is the present surface expression of the MHT, and in the north by the Main Boundary thrust (MBT).

2.2 Lesser Himalaya

In central Nepal, the Lesser Himalaya is made up of eight mappable formations, which can be divided into Paleoproterozoic lower and Mesoproterozoic upper units, with a total thickness of ~8–13 km (Sakai, 1983, 1985; Upreti, 1996; Khanal and Robinson, 2013; Robinson et al., 2021). The lower Lesser Himalaya is made up of two distinct units, the Kuncha and Robang Formations, both of which have been metamorphosed to greenschist (south) and amphibolite (north) facies phyllites and schists (Martin et al., 2011). The basal Kuncha Formation is made up of gray-green quartz- and chlorite-rich phyllite, green quarzitic schist, and micaceous quartzite. Detrital zircons place the maximum depositional age of the Kuncha at ca. 1900 Ma, with the Robang deposited at some point before 1850 Ma and interpreted as an older and more distal facies of the Kuncha (Martin et al., 2011). The Robang is made up of chloritic schist,

[1]Supplemental Material. Text S1 and Figures S1–S4; Tables S1 and S2; and Videos S1–S3. Please visit https://doi.org/10.1130/GEOS.S.25669419 to access the supplemental material, and contact editing@geosociety.org with any questions.

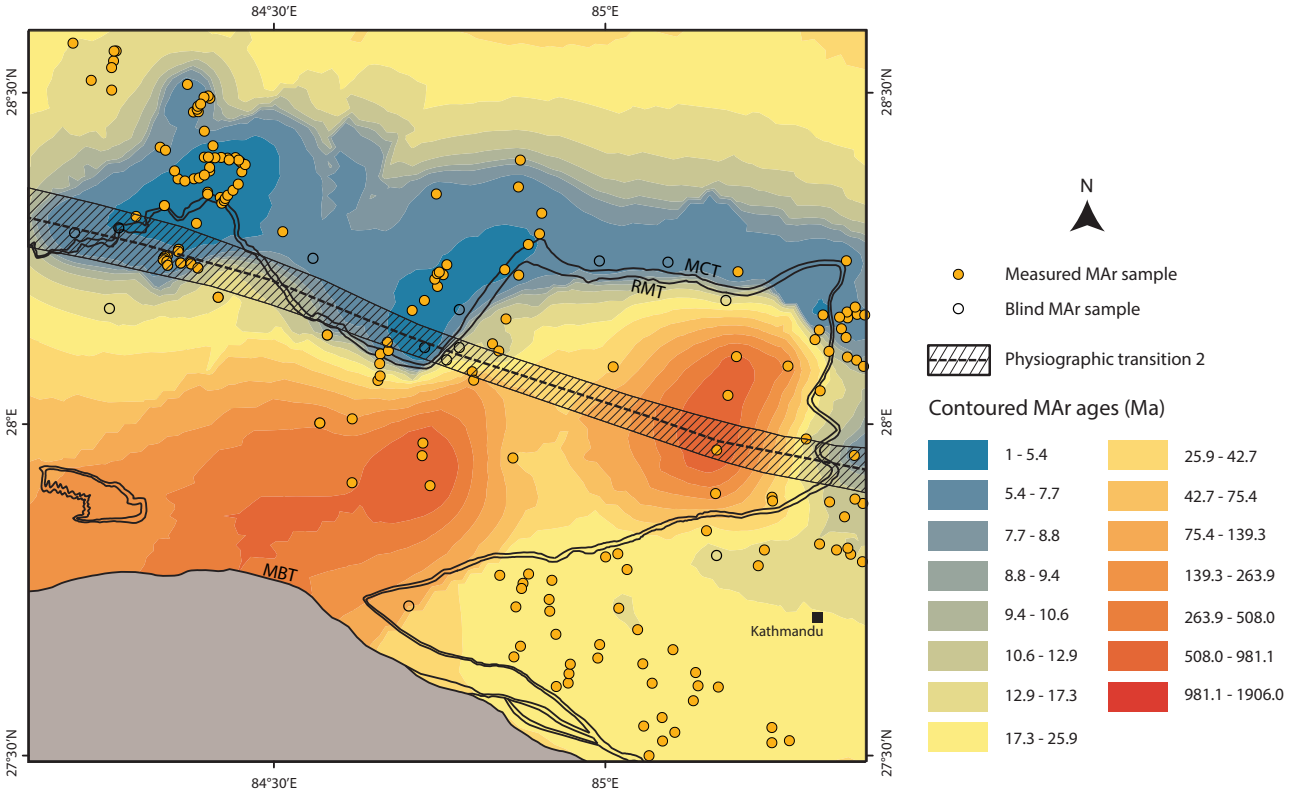

Figure 2. Predictive map of muscovite Ar-Ar (MAr) ages in central Nepal interpolated through a kriging process that produces a narrower contour interval where data density is high and age variation is small. "Blind" samples are either the same age as their nearest neighbor or are the mean of the ages on either side. MCT—Main Central thrust; RMT—Ramgarh-Munsiari thrust; MBT—Main Boundary thrust.

commonly interbedded with a distinctive, white–light green quartzite known as the Dunga quartzite. The base of the Robang is interpreted in central Nepal as the Ramgarh-Munsiari thrust (RMT) (Pearson and DeCelles, 2005; Robinson and Pearson, 2013). The Kuncha forms the core of the Gorkha-Pokhara antiform, exposed between the RMT and MCT in the north, and the MBT in the south. It is overlain by the entire upper Lesser Himalaya, composed of six Paleoproterozoic–Mesoproterozoic units: the Fagfog, Dandagaon, Nourpul, Dhading, Benighat, and Malekhu Formations, metamorphosed to the lower greenschist facies (Upreti, 1996; Martin et al., 2011) (Fig. 1). The Fagfog Formation is a thin (~300 m) unit made up of a tan and/or white, coarse- to fine-grained quartzite, with individual beds commonly separated by green chloritic phyllite. It has a maximum depositional age of ca. 1770 Ma (Martin et al., 2011) and is mapped unconformably over the Kuncha. Overlying the Fagfog, the ~650-m-thick Dandagaon Formation is made up primarily of dark brown to gray-green phyllite interbedded with thin beds of slate and dolomite. The ~450-m-thick Nourpul Formation is made up primarily of thinly bedded variegated quartzite (pink, purple, green, and white) interbedded with blue-gray dolomite, and dark purple and green phyllite, with a silicic dolostone dominating the upper portion of the unit (Pearson, 2002; Olree, 2018). Detrital zircon measurements suggest a maximum depositional age for the Nourpul at ca. 1750 Ma (Cross, 2014). The ~150-m-thick Dhading Formation is made up of massive blue-gray dolomite with a distinctive "butcher block" weathering pattern. The contact between the Dhading and the Benighat Formations is abrupt, with the dolomite changing into dull, dark gray-black slate and thin limestone beds. The Malekhu Formation lies conformably on top of the Benighat and consists of blue-gray limestone and dolostone, interbedded

with gray-black and brown phyllite, and is proposed to have been deposited before ca. 1300 Ma (Martin et al., 2011).

2.3 Greater Himalaya

In central Nepal, the metasedimentary Greater Himalayan sequence is mapped as being ~15–23 km thick, metamorphosed to amphibolite to granulite facies (Colchen et al., 1986; Coleman, 1996; Kohn, 2008; Corrie and Kohn, 2011; Ghoshal et al., 2020, 2023), and made up of layers of biotite and calc-silicate schist, quartzite, and two-mica orthogneiss. The upper portion of the Greater Himalayan sequence comprises diopside-bearing calc-silicate gneiss, below which are granitic orthogneisses, sillimanite-bearing paragneiss, and quartzite intercalated with pelitic gneiss (Colchen et al., 1986; Kohn et al., 2001; Larson et al., 2010). At the bottom of the sequence are interlayered biotite schist, biotite-rich quartzite, and a two-mica (biotite and muscovite) orthogneiss with feldspar augen along with a flat-lying sequence of calc-silicate schists and marble. In the neighboring Marsyangdi valley, the Greater Himalayan sequence has been dated to between 1000 and 600 Ma with early Paleozoic granitic intrusions (Martin et al., 2005; Gehrels et al., 2011). The MCT places the Greater Himalayan sequence onto the rocks of the Lesser Himalaya, defining its base.

3. THERMOCHRONOLOGY

3.1 Regional Thermochronology

We present a compilation of 148 MAr (135 bedrock and 13 detrital) ages, 39 ZHe ages, and 83 AFT ages collected from the Marsyangdi, Daraundi, Budhi Gandaki, and Trishuli valleys of central Nepal (see Table S1 [footnote 1] for a complete list and sources). Alongside the published data are two new ZHe ages (Fig. 1, green triangles with red borders) from the Daraundi valley, with one collected from the Greater Himalaya (sample CN16-162) and the other from the Robang Formation (CN16-168). These analyses were performed at the University of Arizona Radiogenic Helium Dating Laboratory (Tucson, Arizona, USA) (Schmitz and Bowring, 2001; Reiners et al., 2004; Hourigan et al., 2005; Reiners, 2005; Renne et al., 2005; Kuiper et al., 2008). The sample collected from the Greater Himalaya is located ~90 km from the MFT and is dated to 3.18 ± 0.5 Ma, while the sample collected from the Robang is located immediately to the south (~87 km from the MFT), with an age of 2.94 ± 0.1 Ma. In addition to these bedrock ages, we also include a group of 10 detrital MAr ages collected from modern river sediments in tributaries to the Budhi Gandaki, Trishuli, and Daraundi Rivers (Fig. 1, yellow diamonds). The uncertainties in the MAr and AFT ages are represented by 2σ analytical errors, with those AFT ages that were initially reported with 1σ errors shown here as 2σ to maintain consistency. We present the ZHe ages as a mean calculated from the range in ages for individual grains (typically three) and their respective 2σ analytical errors.

3.2 Thermochronology of the Daraundi Valley

We constrain our new cross section along the Daraundi valley with a smaller subset (22 MAr and four ZHe) of cooling ages located within ~15 km of the cross section to eliminate the effect of lateral structures. These cooling ages are then projected onto the cross-section line along strike, maintaining their relative structural positions (Fig. 3A), and plotted with respect to their distance from the trace of the MFT. We also include four detrital MAr age distributions to further constrain our model. The northernmost detrital sample (S40) was collected from the headwaters of the Daraundi River (Brewer et al., 2006). Projected onto the section, the drainage basin for S40 extends from 109 km to 117 km from the MFT, with a 2σ range of ages between 4.5 and 7 Ma. Three more detrital samples (01WBS1, 01WBS2, and 01WBS3) collected from the Kuncha Formation in the south show the distribution of unreset ages over the Gorkha-Pokhara antiform (Wobus et al., 2006).

The bedrock MAr ages in the Daraundi valley range from very young (2.64 Ma) to unreset (398 Ma), with the majority of reset ages located north of the MCT (89 km from the MFT) and the youngest cluster of ages located between 98 and 104 km from the MFT. The northernmost bedrock MAr age (dated to ca. 6.5 Ma) is located 117 km from the MFT, falling within the range of detrital MAr ages measured in sample S40. There are three unreset or partially reset bedrock MAr ages in the transect, all of which were collected from south of the MCT. The southernmost age is also the oldest at 398 Ma, located 66 km from the MFT, with the ages becoming younger toward the north, dated to 257 Ma (~75 km) and 125 Ma (77 km), respectively. Finally, the four measured ZHe ages in the transect range between 2.5 and 4.9 Ma, extending 68–90 km from the MFT. The youngest ZHe age (ca. 2.5 Ma) is located to the north of the MCT (88.5 km from the MFT).

4. METHODS

4.1 Balanced Cross Section

We present a new balanced cross section along the Daraundi valley, integrating newly acquired mapping (Section 5.1) with existing published mapping (Colchen et al., 1986; Catlos et al., 2001; Larson et al., 2010). Measured map orientations were projected onto the line of section, maintaining their structural position, and used to limit permissible geometries. The line lengths of each of the units in the deformed section were measured and balanced in the restored section (Fig. S2, see footnote 1). Small-scale internal deformation (brittle or ductile) within the units is not accounted for in our modeling.

The base of the cross section is defined by the MHT and is divided into three parts: the ramp of the MFT, a broad flat, and a northern mid-crustal ramp (Pandey et al., 1995; Lavé and Avouac, 2001). All of the major faults (e.g., MFT, MBT, MCT, etc.) shown sole into the MHT, transmitting shortening from it to the surface. The ~5 km height of the MFT ramp is defined primarily by the

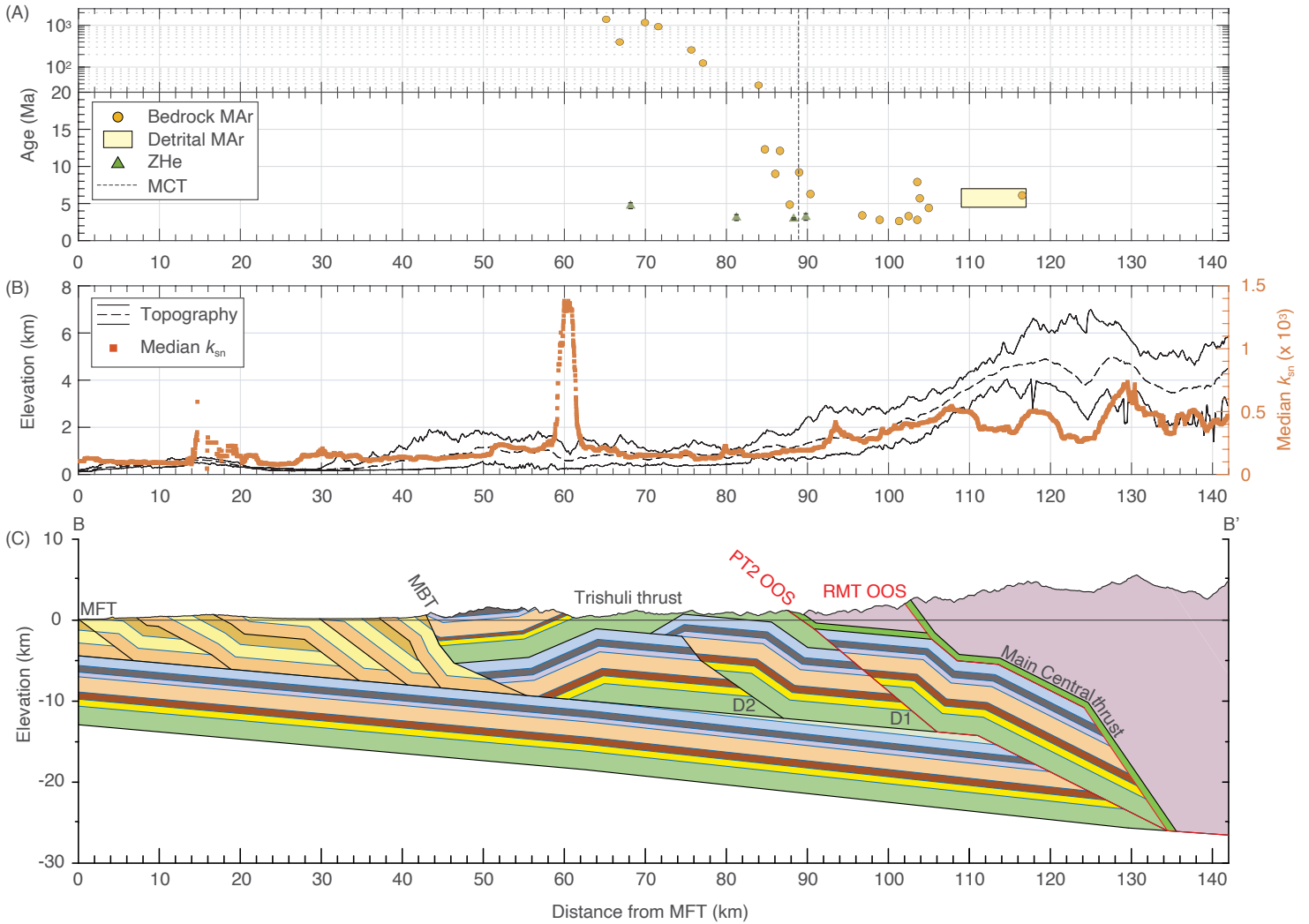

Figure 3. (A) Combined measured muscovite Ar-Ar (MAr) (yellow circles and rectangle) and zircon (U-Th)/He (ZHe) (green triangles) thermochronometer data plotted along the Daraundi section line. Location of the Main Central thrust (MCT) is marked by the black dashed line, while the origin for the distance axis is the location of the Main Frontal thrust (MFT). (B) Maximum and minimum (solid black lines) and mean (dashed black line) swath topography along the Daraundi cross-section line. Median values of normalized stream power index (k_{sn}) calculated along the swath are shown in orange. (C) Balanced cross section along the Daraundi transect. Locations of major out-of-sequence (OOS) thrusts are marked in red (PT2—physiographic transition 2; RMT—Ramgarh-Munsiari thrust). D1, D2—1197 individual horses of the Lesser Himalayan duplex in the order that they deform. There is no vertical exaggeration on the figure, and the topography shown is the mean topographic profile for the transect. MBT—Main Boundary thrust.

thickness and orientation of the exposed Siwalik Group at the surface. This is reinforced by extrapolating the depth and dip of the base of the Siwalik Group measured at the Raxaul drill core (located to the southeast; Sastri et al., 1971). Inversion of seismic data from the Gorkha earthquake provides a narrow range of permissible angles for the MHT flat (4°–8°) (Avouac et al., 2015; Elliott et al., 2016; Whipple et al., 2016). To construct our cross section, we explored décollement angles to find the one that fits the geophysical constraints, the required thickness of Lesser Himalaya units mapped at the surface, and viable repetition of units between the surface geology and décollement. Finally, thermokinematic modeling (Lock and Willett, 2008; McQuarrie and Ehlers, 2015; McQuarrie et al., 2019; Ghoshal et al., 2020, 2023) shows predictive relationships between the location of ramps and the resulting pattern of modeled cooling ages; production of young, reset higher-temperature thermochronometers (e.g., MAr) requires the overlying rocks to be completely translated over a mid-crustal ramp. Therefore, the top of the ramp must be located to the north of the youngest reset ages (Ghoshal et al., 2020). However, due to a lack of sufficient measured thermochronometer ages in the north of the Daraundi valley, we tested a variety of different geometries and locations of the ramp and identified a solution that best matches the distribution of all the available cooling ages.

4.2 Kinematic and Flexural Modeling

Our restored cross section was kinematically and flexurally forward modeled using the structural modeling software Move 2019.1 (Petroleum Experts). The kinematic model is divided into displacement increments of ~10 km and modeled using the fault-parallel flow algorithm. Each of these kinematic increments was followed by flexural loading and erosional unloading. The magnitude of flexural loading for each step is calculated using the difference between (1) the deformed topography resulting from each ~10 km increment of displacement and (2) the estimated topography from the previous step. We use a "responsive topography" method to calculate the amount of erosion at each step, where the new eroded topography is defined by a taper angle (2°) that increases in elevation toward the north (McQuarrie and Ehlers, 2015; Gilmore et al., 2018). This angle is based on the taper angle of modern topography in central Nepal and accommodates erosion where active uplift has exceeded the 2° slope. In locations where no uplift has occurred, the new topography follows the existing, isostatically loaded topography. This "responsive topography" method creates steepened topography over locations of active uplift, even though the first-order taper angle (2°), above which rocks are eroded, stays constant. The locally steep topography is created because uplift is focused across discrete regions above active ramps spanning 5–50 km. This approach creates a modeled topography that mimics (to a first order) measured topographic profiles (e.g., Braza and McQuarrie, 2022; Ghoshal et al., 2023). The initial topography for the model is represented by a steady increase (2°) in elevation toward the north, reaching a maximum elevation of 5 km above the southern limit of the Greater Himalaya. This simplified topography reproduces the elevation of the Tibetan Plateau, which is thought to have reached its modern elevation by the late Oligocene (DeCelles et al., 2007).

Prior to any deformation in our models, we use our best-fit estimate for the initial geometry of the Indian margin to define the original dip of the décollement. We use an angle of 1.5° as this original sedimentary taper, applied from the foreland to the northern extent of the model. This angle allows us to reproduce the ~15 km section of Tethyan rocks exposed in southern Tibet (Brookfield, 1993; Ratschbacher et al., 1994; Zhang and Guo, 2007) and facilitates the burial of the initial base of the Greater Himalaya section to ~45 km to match measured values of peak pressure and temperature (Kohn et al., 2001, 2004; Catlos et al., 2001, 2018; Kohn, 2008). The building of topography and subsequent erosion occurring at each increment in the models flexurally steepens the décollement and increases the depth of the foreland basin. The final dip and depth of the décollement are dependent upon three parameters (i.e., effective elastic thickness, crustal density, and the initial dip of the décollement) that are systematically varied until the surface geology and expected foreland basin depth are replicated. The best-fit values and ranges (if any) for these parameters are listed in Table 1.

The kinematic and flexural forward model is tracked using a two-dimensional grid of points with a resolution of 0.5 km that is deformed sequentially at

TABLE 1. MECHANICAL AND THERMAL PARAMETERS FOR THE THERMOKINEMATIC MODEL

Parameter	Input value
Initial dip of décollement	1.5°
Material properties	
Effective elastic thickness	70 km
Crustal density	2950 kg m^{-3}
Mantle density	3300 kg m^{-3}
Specific heat capacity	800 J kg^{-1} K
Surface radiogenic heat production (A_0)	2.15–2.35 μW m^{-3}
e-folding depth	20 km
Thermal conductivity	2.5 W m^{-1} K
Numerical properties	
Temperature at base of model	1300 °C
Model thickness	110 km
Surface temperature	20 °C
Atmospheric lapse rate	7 °C km^{-1}
Kinematic grid spacing	0.5 km
Horizontal node spacing	0.5 km
Vertical node spacing	1 km
Model domain	1000 km × 110 km × 5 km
Model start time	500 Ma

Notes: The best-fit values for the material properties were selected through iterative modeling until the models were able to match various independently measured quantities (e.g., decollement angle, surface geology, topography, and thermochronological ages).

each increment. Assigning an age to each step of the model converts the displacement field into a velocity field, which is then input into a modified version of Pecube (Braun, 2003), known as Pecube-D (Whipp et al., 2007; McQuarrie and Ehlers, 2015; Ehlers, 2023). While we initially test the model with a constant rate of shortening (20 mm yr^{-1}), varying the ages at which faults are initiated allows us to assign variable rates of thrusting and quantify their effects on the predicted cooling ages. Using this approach, we also evaluate a range of potential velocity profiles, with individual thrust sheets moving at velocities within India-Eurasia convergence rates (35–40 mm yr^{-1}; Bettinelli et al., 2006), ranging from 6.7 mm yr^{-1} to 37.7 mm yr^{-1}, with the best-fit profile listed in Table 2. In addition, due to its proximity to the neighboring Marsyangdi and Budhi Gandaki transects, the velocities proposed for the Daraundi transect also needed to be consistent with those identified along those transects (Table 3). We present the results here for the best-fit velocity profile, which is consistent with the velocities identified for the kinematic models along the Budhi Gandaki and Marsyangdi transects (e.g., Ghoshal et al., 2020, 2023) (Table 3; Fig. S4).

TABLE 2. VELOCITY PROFILES FOR FINAL DARAUNDI MODELS

Structure	Shortening (km)	Constant rate		Best-fit rates	
		Initiation (Ma)	Rate (mm yr^{-1})	Initiation (Ma)	Rate (mm yr^{-1})
MCT_start	150	23.00	19.79	23.00	21.58
MCT_end	21	15.42	19.79	16.05	14.06
RMT_start	50	14.36	19.79	14.56	14.06
RMT_end	54	11.83	19.79	11.00	19.34
TT_start	40	9.10	19.79	8.21	16.76
TT_end	50.5	7.08	19.79	5.90	26.67
D1	11.8	4.53	19.79	3.94	22.75
D2	10	3.93	19.79	3.42	22.75
Siw1	8	3.43	19.79	2.98	22.75
Siw2	10.5	3.02	19.79	2.63	22.75
Siw3	17.4	2.49	19.79	2.17	22.75
Siw4	11.9	1.61	19.79	1.40	22.75
RMT OOS	10	1.01	19.79	0.88	22.75
PT2 OOS	5	0.51	19.79	0.44	22.75
Siw1 OOS	2	0.25	19.79	0.22	22.75
MFT	3	0.15	19.79	0.13	22.75

Notes: MCT—Main Central thrust; RMT—Ramgarh-Munsiari thrust; TT—Trishuli thrust; D1, D2—thrusts that construct the Lesser Himalayan Duplex, numbered in the order of their activation; Siw1–Siw4—intra-siwalik thrust faults numbered in order of their activation; MFT—Main Frontal thrust; OOS—out-of-sequence faults; RMT OOS—reactivated Ramgarh-Munsiari thrust; PT2 OOS—out-of-sequence fault surfacing at the Physiographic Transition 2; Siw1 OOS—reactivated motion on Siw1. Motion on the major large displacement faults were broken up into segments to fine-tune the thermochronological fit to the ages; _start and _end represent the two segments motion of these faults. Best-fit times and rates shown here are able to produce the best fit to the measured thermochronological ages.

4.3 Thermokinematic Modeling

Pecube (Braun, 2003) solves the three-dimensional heat transport equation to simulate the evolution of a transient thermal field defined by crustal and mantle thermal parameters, translation of crustal material, and surface erosion. The model uses the evolving temperature field to calculate time-temperature (*t-T*) paths for the rocks at the surface, which are then used by age-prediction algorithms to predict the surface cooling ages for each of the tracked points at the surface (Braun, 2003; Ehlers et al., 2005). Instead of using fixed closure temperatures, the closure temperature, the model calculates the closure temperature for each system based on published models for mineral kinetics and the rate of cooling. The MAr kinetics are based on the thermally activated diffusion model as set out in Dodson (1973), using the parameters defined in Hames and Bowring (1994) for cylindrical geometries (Hodges, 2014). The ZHe kinetic model is defined in Reiners et al. (2004), while the AFT ages are calculated using the parameters given in Ketcham et al. (2007).

Pecube-D (Ehlers, 2023), a modified version of the original Pecube (Braun, 2003), simulates the thermal state of the crust using the input values of heat flow from the mantle, the material properties of the crust (thermal conductivity, density, heat capacity, and radiogenic heat production), imported velocity grids, and modeled topographic surfaces (McQuarrie and Ehlers, 2015; Tables 1 and 2). Our models start at 500 Ma to create a steady-state thermal field (no velocity) before faulting, and the resulting displacement initiates at 23 Ma. The 500 Ma model start time also facilitates a permissible range of partially reset cooling ages from 500 to 23 Ma. The amount of heat generated in the crust is determined by a surface radiogenic heat production value (A_0), which is at a maximum at the surface and decays exponentially to 1/e of the assigned surface value (McQuarrie and Ehlers, 2017). The distance over which the radiogenic heat production value decays is referred to as the "e-folding depth" (McQuarrie and Ehlers, 2017). Using a surface radiogenic heat production value (A_0) and associated e-folding depth allows our models to replicate both the measured nonlinear decline of heat production in the crust with depth (Ketcham, 1996; Menon et al., 2003; Brady et al., 2006) and measured heat production values for the Himalaya and similar lithologies found elsewhere (England et al., 1992; Whipp et al., 2007), while also avoiding the formation of partial melt in the middle and lower crust. While crustal material properties (e.g., heat production, thermal conductivity, and thermal capacity) are not advected by the imposed displacement fields and remain static throughout our simulations, the resulting crustal thermal field evolves through time due to advection of material and surface erosion (Ghoshal et al., 2020, 2023; Braza et al., 2023).

We tested the sensitivity of predicted cooling ages to assigned thermal properties by systematically varying the surface radiogenic heat production value between 2.00 and 3.00 μW m^{-3} to find values that can reproduce the best-fit cooling signal using an e-folding depth of 20 km. The values of thermal conductivity and heat capacity used in our models are consistent with measured values from the Himalaya (Ehlers et al., 2005; Whipp et al., 2007;

TABLE 3. FINAL VELOCITY PROFILES FOR THE MARSYANGDI, DARAUNDI, AND BUDHI GANDAKI TRANSECTS

Structure	Marsyangdi			Daraundi			Budhi Gandaki		
	Shortening (km)	Initiation (Ma)	Rate (mm yr^{-1})	Shortening (km)	Initiation (Ma)	Rate (mm yr^{-1})	Shortening (km)	Initiation (Ma)	Rate (mm yr^{-1})
MCT	148	23.00	21.29	150	23.00	21.58	147	23	21.15
RMT_start	70	16.05	14.40	71	16.05	14.06	70	16.05	15.73
RMT_end	72.5	11.19	20.71	64	11.00	19.34	70	11.6	17.07
TT_start	31	7.69	16.85	30	7.69	16.76	30	7.5	16.39
TT_end	40	5.85	22.86	40	5.9	26.67	–	–	–
D1	5	4.10	21.61	11.8	3.94	22.75	38.3	5.67	31.39
D2	15	3.87	21.61	10	3.42	22.75	16.95	4.45	25.11
D3	–	–	–	–	–	–	6.679	3.78	25.11
D4	–	–	–	–	–	–	60	3.51	25.11
Siw1	8	3.17	21.61	8	2.98	22.75	–	–	–
Siw2	13.2	2.80	21.61	10.5	2.63	22.75	–	–	–
Siw3	13.9	2.19	21.61	27.4	2.17	22.75	–	–	–
Siw4	9.6	1.55	21.61	11.9	1.40	22.75	8	1.12	25.11
RMT OOS	10	1.11	21.61	10	0.88	22.75	5	0.80	25.11
PT2 OOS	5	0.64	21.61	5	0.44	22.75	5	0.60	25.11
Siw1 OOS	2	0.41	21.61	2	0.22	22.75	2.8	0.40	25.11
MFT	6.9	0.32	21.61	3	0.13	22.75	7.3	0.29	25.11

Notes: MCT—Main Central thrust; RMT—Ramgarh-Munsiari thrust; TT—Trishuli thrust; D1, D2—thrusts that construct the Lesser Himalayan Duplex, numbered in the order of their activation; Siw1–Siw4—intra-siwalik thrust faults numbered in order of their activation; MFT—Main Frontal thrust; OOS—out-of-sequence faults; RMT OOS—reactivated Ramgarh-Munsiari thrust; PT2 OOS—out-of-sequence fault surfacing at the Physiographic Transition 2; Siw1 OOS—reactivated motion on Siw1. Motion on the major large displacement faults were broken up into segments to fine-tune the thermochronological fit to the ages; _start and _end represent the two segments motion of these faults. D3 and D4 are not present in the Daraundi and Marsyangdi transects.

Ray et al., 2007). The best-fit parameters used to set up the thermal model in Pecube-D are listed in Table 1. We assessed our model's ability to fit data by determining the percentage of measured ages that match the modeled data using the method outlined in Braza and McQuarrie (2022) (Text S1, section 3, see footnote 1). In brief, a match occurs when a modeled age (including a ±0.5 m.y. error) overlaps a measured age from the same system, accounting for a spatial error of ±0.5 km due to uncertainties in data projection and the data measurement error (±2σ, m.y.). We report the matches as a percentage of the total number of ages and individual fits for each system.

5. RESULTS

5.1 Along-Strike Variations in Surface Geology

Fieldwork along the Daraundi valley reveals a marked change in the latitude of the MCT between the Daraundi and Budhi Gandaki River valleys. In the Budhi Gandaki and Marsyangdi valleys, the RMT and MCT thrust sheets are located on top of the entire upper Lesser Himalayan sequence, which in turn rests on top of the lower Lesser Himalaya Kuncha Formation (Khanal and Robinson, 2013; Ghoshal et al., 2020, 2023) (Fig. 1). However, new mapping in the Daraundi valley diverges from this, with the visually distinct chlorite-garnet schist and white quartzite of the Paleoproterozoic Robang Formation (DeCelles et al., 2000; Pearson and DeCelles, 2005) located structurally above the Kuncha. Approximately 800 m to the north of the Robang, we observed interlayered biotite and calc-silicate schist, biotite-rich quartzite, and a two-mica (biotite and muscovite) orthogneiss with feldspar augen. Traces of partial melt can be found within the biotite schist, suggesting that this is within the immediate hanging wall of the MCT. This new location of the MCT is ~30 km farther south than that mapped in the Budhi Gandaki and Marsyangdi valleys (Ghoshal et al., 2020, 2023). It is also ~10 km farther south along the Daraundi River than mapped in the past (Colchen et al., 1986; Catlos et al., 2001), coinciding with the trace of the MCT-I thrust from Catlos et al. (2001).

In the Marsyangdi valley to the west, out-of-sequence (OOS) thrusting has been proposed for the RMT-MCT zone to explain the concentration of young, reset cooling ages north of this zone (Harrison et al., 1997; Catlos et al., 2001, 2018; Hodges et al., 2004; Huntington et al., 2006). Integrating cross-section geometry and thermokinematic modeling highlights that ~10 km of OOS faulting along the RMT-MCT zone is required to reproduce young AFT cooling ages ~150–160 km north of the MFT (Ghoshal et al., 2023). Faulting of this magnitude in the Marsyangdi is expected to be present in the closely neighboring Daraundi valley as well. Approximately 10 km north of the newly

mapped trace of the MCT is clean white quartzite, which was mapped by Colchen et al. (1986) as part of the Lesser Himalaya, contiguous with the Robang Formation in the Budhi Gandaki valley (Fig. 1; Fig. S3A, see footnote 1). This quartzite and its along-strike extension align with the proposed OOS fault in the Marsyangdi valley and support additional OOS faulting in the RMT-MCT zone along the Budhi Gandaki valley. We suggest that this quartzite is a repetition of the Robang due to an OOS thrust connecting the traces of the RMT in the Budhi Gandaki and Marsyangdi transects and closely following the trace of the Chomrong thrust as shown in Parsons et al. (2016) (Fig. 1). Motion on this OOS thrust is responsible for steepening the dips farther north from horizontal to 25°N–54°N (Fig. 1). Farther north, undisputed Greater Himalayan paragneiss lies above a sequence of marble and diopside-bearing calcsilicate (Colchen et al., 1986; Catlos et al., 2001; Larson et al., 2010).

With field mapping confined mostly to the valleys, we use satellite imagery to project the surface traces of the MCT and RMT from the Budhi Gandaki and Marsyangdi valleys to the Daraundi valley. We processed multiple Advanced Spaceborne Thermal Emission and Reflection Radiometer (ASTER) images to highlight specific units, relying on the different reflectance of a variety of minerals in the infrared region of the electromagnetic spectrum. While vegetation and snow cover complicate this analysis, we were able to identify high concentrations of chlorite (Fig. S3B), which we interpret to be indicative of the Robang Formation. Further analysis of these images in the thermal infrared bands allowed us to distinguish between distinctly carbonaceous rocks and silicic rocks, highlighting the southwestern extent of the Lesser Himalaya carbonates that have been observed in the Budhi Gandaki valley (Fig. S3C).

5.2 Balanced Cross Section along the Daraundi Valley

5.2.1 Subhimalayan Faults

The MFT ramp is proposed to dip at an angle of ~30°N, with an approximate depth of 5 km. This depth and dip are consistent with mapped upper through lower Siwalik Group thicknesses at the MFT (Fig. 3) and the depth of the Siwalik basement as defined by the Raxaul drill hole (Sastri et al., 1971).

In central Nepal, the area over which the Siwalik Group is exposed (i.e., the Subhimalayan zone) increases systematically from the Budhi Gandaki valley to the west. Along the Daraundi transect, Siwalik units are exposed over an ~43 km distance from the MFT to the MBT. This area gain is primarily a combination of two factors: (1) the MFT surfacing ~15 km farther to the south in the Daraundi valley and ~20 km farther south in the Marsyangdi valley and (2) the MBT surfaces ~7 km and ~10 km farther north within the Daraundi and Marsyangdi valleys, respectively, than in the Budhi Gandaki (Fig. 1). The three-part sequence of the Siwalik Group goes through four asymmetric repetitions of lower to upper Siwalik along both the Marsyangdi (e.g., Ghoshal et al., 2023) and Daraundi transects (Fig. 1). Similar to its exposure in the Marsyangdi transect, the middle Siwalik member is exposed over an ~10 km stretch of the Daraundi transect between 20 and 33 km from the MFT, with measured dips between ~20°N and 25°N. When combined with the ~2 km measured thickness of the middle Siwalik member, the conclusion that this is one single thrust sheet becomes inconsistent. Therefore, we follow the interpretation made along the Marsyangdi (e.g., Ghoshal et al., 2023) and divide this segment into two separate thrust sheets, with the lower sheet carrying only the lower and middle Siwalik members and the top sheet carrying the middle and upper.

5.2.2 Main Boundary Thrust

In the Daraundi transect, the MBT places the Dhading Formation and the underlying rocks of the Lesser Himalaya against the Siwalik Group to the south (Figs. 1 and 3). In the Marsyangdi and Budhi Gandaki valleys, Siwalik Group rocks south of the MBT and Lesser Himalaya rocks immediately north of the MBT dip 40°–66° toward the north. Using the mapping in these two valleys and published mapping from the Siwalik Group of the Bagmati region (south of Kathmandu; Dhital, 2015), we estimate the approximate dip of the rocks to the immediate north of the MBT to be ~45°N and interpret these rocks to flatten immediately to the north.

5.2.3 Trishuli Thrust and the Gorkha-Pokhara Antiform

Along the Daraundi section and to the east, the surface trace of the MBT is also the surface trace of the Trishuli thrust (TT), which underlies and displaces the entire Lesser Himalaya section (Ghoshal et al., 2020, 2023). Rocks carried by the TT sheet are deformed into a synform, with the Benighat Formation at its core (Fig. 1). To create the geometry of the synform in the Daraundi, we project dips measured along the Marsyangdi and Budhi Gandaki valleys along strike onto the line of section while remaining consistent with the mapped changes in geology. Projecting these measurements onto the section suggests that the 54°N–25°N mapped dips to the west are expressed in the Daraundi section as a 25°N–40°N dip for the southern limb of the synform. The rocks exposed in the broader northern limb of the synform dip southwards between 18°S and 23°S. The northern limb of the synform exposes the Dhading Formation and lower Lesser Himalaya section down to the Kuncha Formation. The Kuncha forms the core of the Gorkha-Pokhara antiform, a major E-W–trending antiformal structure mapped across central Nepal (Fig. 1). In the Daraundi valley (Section 5.1), the RMT and MCT lie directly on top of the Kuncha, with the trace of the RMT cutting across the upper Lesser Himalaya units 9.5 km to the east and 6 km to the west of the Daraundi River (Fig. 1). We argue that this represents a lateral ramp system that offsets upper Lesser Himalaya rocks from lower Lesser Himalaya rocks (i.e., Kuncha) during the emplacement of the RMT (Fig. 3; Fig. S2).

Across central Nepal, the Gorkha-Pokhara antiform is interpreted to represent a subsurface duplex (e.g., Pandey et al., 1995; Lavé and Avouac, 2001;

Pearson, 2002; Avouac, 2003; Khanal and Robinson, 2013; Khanal, 2014; Robinson and Martin, 2014; Hubbard et al., 2016; Ghoshal et al., 2020, 2023) whose geometry is obscured at the surface by the rocks of its roof thrust (i.e., the TT sheet). Along the Budhi Gandaki and Marsyangdi transects, sequential thermokinematic modeling of the cross-section geometries shows that the duplex comprises hinterland-dipping horses that repeat the entire Lesser Himalayan sequence, which is then translated over the modern MHT ramp (Ghoshal et al., 2020, 2023). In both of these transects, the youngest horse of the duplex must carry rocks that are derived from the active ramp and therefore has a thickness that corresponds to the ramp height (Ghoshal et al., 2020, 2023). Along the Daraundi valley, the height of the modern ramp and the architecture of the duplex are both unknown. However, the geometry of the duplex is limited by the space created between the rocks at the surface and viable décollement depths below.

The youngest MAr ages (2–3 Ma) along the Daraundi valley are located between 98 and 104 km north of the MFT (Fig. 3), suggesting that the top of the modern MHT ramp must be located farther to the north. Although limited in their northern extent, an isolated MAr bedrock age of 6.1 Ma and detrital MAr ages that range from 4.5 to 7 Ma suggest that the top of the ramp lies to the north of these samples, between 104 and 114 km from the MFT. Because the lack of cooling ages farther north prevents us from directly inferring the location of the bottom of the ramp and, therefore, its height, we evaluated a range of ramp locations and geometries along with various duplex geometries capable of filling the available space above the décollement. The final duplex geometry comprises two horses, both carrying a thickness of ~9 km of Lesser Himalaya material (upper Lesser Himalaya + Kuncha Formation). Because the rocks making up the youngest horse of the duplex are derived from the active ramp, this suggests that the modern ramp is ~9 km high. Combining the estimated height of the ramp (~9 km) with reasonable angles of dip (20°N–30°N) allows us to predict a ramp length of ~20 km.

5.2.4 Ramgarh-Munsiari and Main Central Thrust Sheets

In the Daraundi valley, rocks within the RMT, i.e., Robang Formation, dip ~39°N, with the structurally higher Greater Himalayan rocks within the immediate hanging wall of the MCT similarly dipping ~40°N. However, these moderately steep dips are limited to within 3–4 km of the RMT before apparent dips become largely horizontal until ~100 km from the MFT. These near-horizontal dips strongly suggest a footwall flat in the décollement as well as within the underlying Lesser Himalaya stratigraphy. North of 100 km, we interpret the repetition of a clean, white quartzite (Colchen et al., 1986) and a change to steeper dips as indicating a structural repetition of the RMT and MCT by a steeply dipping OOS thrust similar to that proposed for the Marsyangdi valley (Ghoshal et al., 2023). Finally, rocks in the upper Daraundi valley (>130 km from the MFT) continue to become significantly steeper, with dips increasing from 24°N to 45°N–52°N. These steeper dips cannot have been generated by the dip of the modern ramp (20°N), suggesting that the rocks have been steepened by the stacking of two ramps. We interpret this as the footwall ramp of the second horse of the duplex, with the top edge of the ramp located ~125 km from the MFT.

While the Robang Formation and Greater Himalayan sequence are not exposed south of the Gorkha-Pokhara antiform in the Daraundi valley, they are exposed in the Kathmandu synform to the east and the Damauli klippe to the west. Similar to the geometry shown in the cross sections along the Marsyangdi and Budhi Gandaki valleys, the RMT carried the entire section of the Robang and Greater Himalayan sequences. Prior to initiation of the TT, the Lesser Himalaya rocks within the TT sheet were buried by the emplacement of the RMT.

5.3 Predicted Cooling Ages

In this section, we present the effect of the Daraundi valley cross-section geometry on predicted cooling ages using a best-fit value for the surface radiogenic heat production (A_0 = 2.35 μW m^{-3}) and thrusting velocities (Table 2) that are consistent with the best-fit models for the Budhi Gandaki and Marsyangdi transects (Table 3). Our models are started at 500 Ma, with no imposed kinematic deformation until 23 Ma, beginning with motion on the MCT.

The MCT is first emplaced onto the Robang Formation, moving over an ~25-km-high ramp (Video S1, steps 1–16, see footnote 1). The resulting erosional exhumation produces reset AFT, ZHe, and MAr cooling ages, with the youngest ages located at the top of the ramp (~420 km) and ages becoming progressively older toward the south. Beginning at 16 Ma, the RMT is emplaced over the rocks that will become the TT sheet. The footwall cutoff of the TT is divided into two smaller ramps that are connected by an ~6 km wide flat. The lower ramp is 4 km high, with the RMT being emplaced over the lower Lesser Himalaya Kuncha Formation (currently located at ~240 km). After moving over the flat, the RMT is then translated onto the upper Lesser Himalaya over an ~7-km-high ramp. This uplift and exhumation resets AFT ages, with the youngest ages predicted over the ramp through upper Lesser Himalaya strata, with the predicted ages becoming progressively older toward the south. While the modeled AFT ages record the emplacement of the RMT, the MAr ages still only record the emplacement of the MCT. The predicted ZHe ages at the former surface partially record both periods of cooling and become ~2 m.y. younger due to motion over the upper Lesser Himalaya ramp. Beginning at 7 Ma, the TT is emplaced on top of the Lesser Himalaya rocks that become the horses of the Lesser Himalaya duplex, moving over an ~9-km-high ramp (located at ~190 km from the MFT) that cuts across the entire Lesser Himalayan sequence. This exhumation predicts reset ZHe and AFT ages above the ramp, continuing till 4.6 Ma, with the hanging-wall cutoff of the TT being emplaced onto the rocks that become the Siwalik Group at the MBT. This translation also results in the footwall edge of the TT sheet (i.e., the active ramp during the emplacement of the RMT) being brought over the new ramp. Continued

exhumation associated with this translation resets MAr ages above the TT. The duplex starts to form at 4.6 Ma, promoting exhumation at the surface, steadily removing the Greater Himalayan rocks overlying it as the duplex is translated southward over the ramp. This exhumation results in the formation of a zone of unreset MAr ages in Lesser Himalaya rocks that are now exposed in the core of the Gorkha-Pokhara antiform above the duplex. Translation of the duplex over the modern MHT ramp begins at 3.2 Ma, when deformation steps into the Siwalik Group, modeling ZHe and AFT ages that steadily increase in age toward the south, with the youngest ages located at the ramp.

Deformation in the Siwalik Group is interrupted at ca. 1 Ma by 10 km of OOS thrusting located ~105 km from the MFT that repeats the Robang Formation and MCT. Exhumation associated with this thrusting exposes younger modeled MAr ages and resets ZHe and AFT ages immediately to the north, creating an inflection point in the predicted ages at 105 km from the MFT (Video S1, step 46). This OOS thrusting is immediately followed by reactivation along the original trace of the RMT, surfacing 90 km from the MFT. Erosional exhumation associated with this motion produces ZHe and AFT ages that are ~1 m.y. younger than before the motion. Active deformation jumps southward to deform the MFT and translate the duplex over the modern ramp as suggested by river incision rates derived from Holocene terraces in central Nepal (Lavé and Avouac, 2001).

At the end of the sequential model, the youngest MAr ages (ca. 2–3 Ma) are predicted between 97 and 106 km from the MFT, correctly reproducing the youngest measured MAr ages in the Daraundi valley. Farther north, the model predicts a swath of reset MAr ages (ca. 4.5–7 Ma) between 108 and 119 km from the MFT, consistent with the range of ages measured within the detrital sample collected from the headwaters of the Daraundi River and matching the single measured bedrock age located ~116 km from the MFT. The model also successfully reproduces the zone of unreset and partially reset ages located to the south of ~88 km, modeling unreset ages in locations where the measured MAr ages are between 1903 and 247 Ma. Finally, the model is also able to successfully reproduce the distribution of ZHe ages, from the young (ca. 1 Ma) ages located between 102 and 130 km to the steady southward increase in the measured ages (between 68 and 90 km) south of the trace of the MCT. This leads to a final overall fit of 85.7% (MAr: 83.9%, ZHe: 100%), meaning that ~86% of the measured MAr and ZHe ages overlapped with predicted ages from our best-fit model, taking into account spatial and measurement errors.

6. DISCUSSION

6.1 Kinematic Evolution of the Central Nepal Himalaya

Combining the kinematic models for the Marsyangdi, Daraundi, and Budhi Gandaki transects (Fig. 4) allows us to evaluate how the geometry of the MHT has changed with time in central Nepal and how these changes have affected the development of the surface geology and exhumed cooling ages. Figure 5 shows the kinematic evolution of the central Nepal Himalaya over five important stages of development and highlights the effects of the resulting geometry and kinematics on the predicted cooling ages.

The models begin with motion on the MCT at ca. 23 Ma, followed by the RMT at ca. 16 Ma. Emplacement of the RMT ends ca. 8 Ma, completely burying the rocks that will later become the TT and exposing Greater Himalayan rocks at the surface (Fig. 5A). Along the Daraundi transect, the footwall ramp over which the RMT is emplaced offsets the upper from the lower Lesser Himalaya, allowing the Robang Formation to be placed directly over the Kuncha Formation (Fig. 5A, i). The footwall ramp itself is located 80–100 km farther south than in the neighboring Budhi Gandaki and Marsyangdi transects, implying that the uplift and exhumation associated with the emplacement of the RMT is concentrated farther to the south within the Daraundi transect, predicting young AFT ages ~220 km from the southern end of the transect, compared to ~300 km and ~340 km for the Marsyangdi and Budhi Gandaki transects, respectively (Fig. 5A, ii and iii). Figure 5B shows how emplacement of the TT sheet between ca. 7 and 8.5 Ma shifts the locus of exhumation ~120 km southwards along the Marsyangdi and Budhi Gandaki transects and begins to passively fold the Greater Himalayan rocks above it. The exhumation generated by the translation over the ramp completely resets the AFT and ZHe ages but is insufficient to completely reset the MAr ages, predicting ages that are only 1–2 m.y. younger than before translation (Fig. 5B, i). While the TT accommodates ~70 km and 90 km of motion in the Marsyangdi and Daraundi transects, respectively, it accommodates only 50 km in the Budhi Gandaki transect. Figure 5B (ii) highlights the Budhi Gandaki section geometry just prior to continued southward translation of the TT by initiation and growth the duplex. Approximately 40 km of additional translation of the TT is coeval with displacement on the first two horses of the Lesser Himalaya duplex (Fig. 5C, D1 and D2). In the Marsyangdi and Daraundi transects, construction of the duplex begins at ca. 4 Ma, coinciding with the initiation of the third horse (D3) of the duplex in the Budhi Gandaki transect (Fig. 5C, i). Motion on a backthrust in the Marsyangdi transect exposes Lesser Himalaya rocks (i.e., part of the TT sheet) at the surface (Fig. 5C, ii). As the duplex develops (in all three sections), the southward migration of the active ramp creates a southward-younging pattern of predicted ZHe and AFT ages. In addition, erosional exhumation occurring above the duplex produces a pattern of MAr ages that were reset by earlier exhumation events during the emplacement of the TT sheet. The horses of the Lesser Himalaya duplex begin to move over the modern ramp at ca. 3.2 Ma, lifting the overlying rocks of the TT, RMT, and MCT sheets (Fig. 5D). In the Marsyangdi and Daraundi transects, this translation places Lesser Himalaya rocks over the footwall of the Siwalik Group (i.e., along the MBT), erosionally removing all Greater Himalayan rocks in the south (Fig. 5D, i). In the Budhi Gandaki transect, the trace of the active MBT is located ~50 km farther to the south, creating a zone of translation and limited exhumation between the duplex and the MBT. This region of low structural elevation between the duplex and the MBT facilitates the formation of the Kathmandu synform and the associated erosional preservation of Greater Himalayan rocks in the south

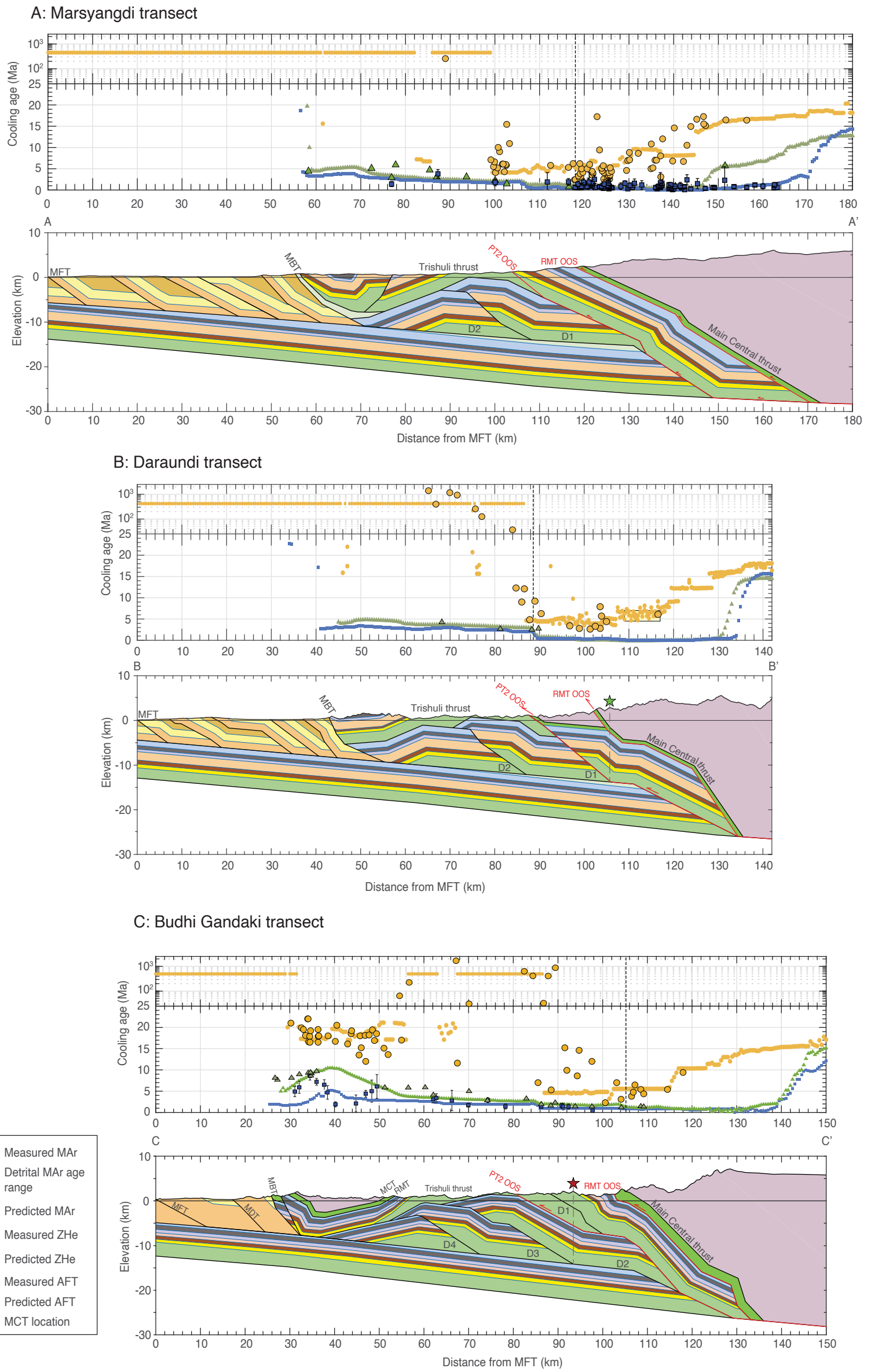

Figure 4. Best-fit geometries for the three transects and their measured versus modeled thermochronological data positioned with respect to the location of the Main Frontal thrust (MFT). (A) Marsyangdi transect. (B) Daraundi transect. (C) Budhi Gandaki transect. Muscovite Ar-Ar (MAr) (yellow circles), zircon (U-Th)/He (ZHe) (green triangles), and apatite fission track (AFT) (blue squares) age data are shown. Error bars show ±2σ. Dashed black line represents the location of the Main Central thrust (MCT) in each of the transects. MDT—Main Dun thrust; MBT—Main Boundary thrust; OOS—out-of-sequence; RMT—Ramgarh-Munsiari thrust; PT2—physiographic transition 2; D1, D2, D3, D4—faults that compose the Lesser Himalayan duplex in order of their initiation. Green star shows Gorkha earthquake epicenter; red star, high-frequency seismic source (Avouac et al., 2015).

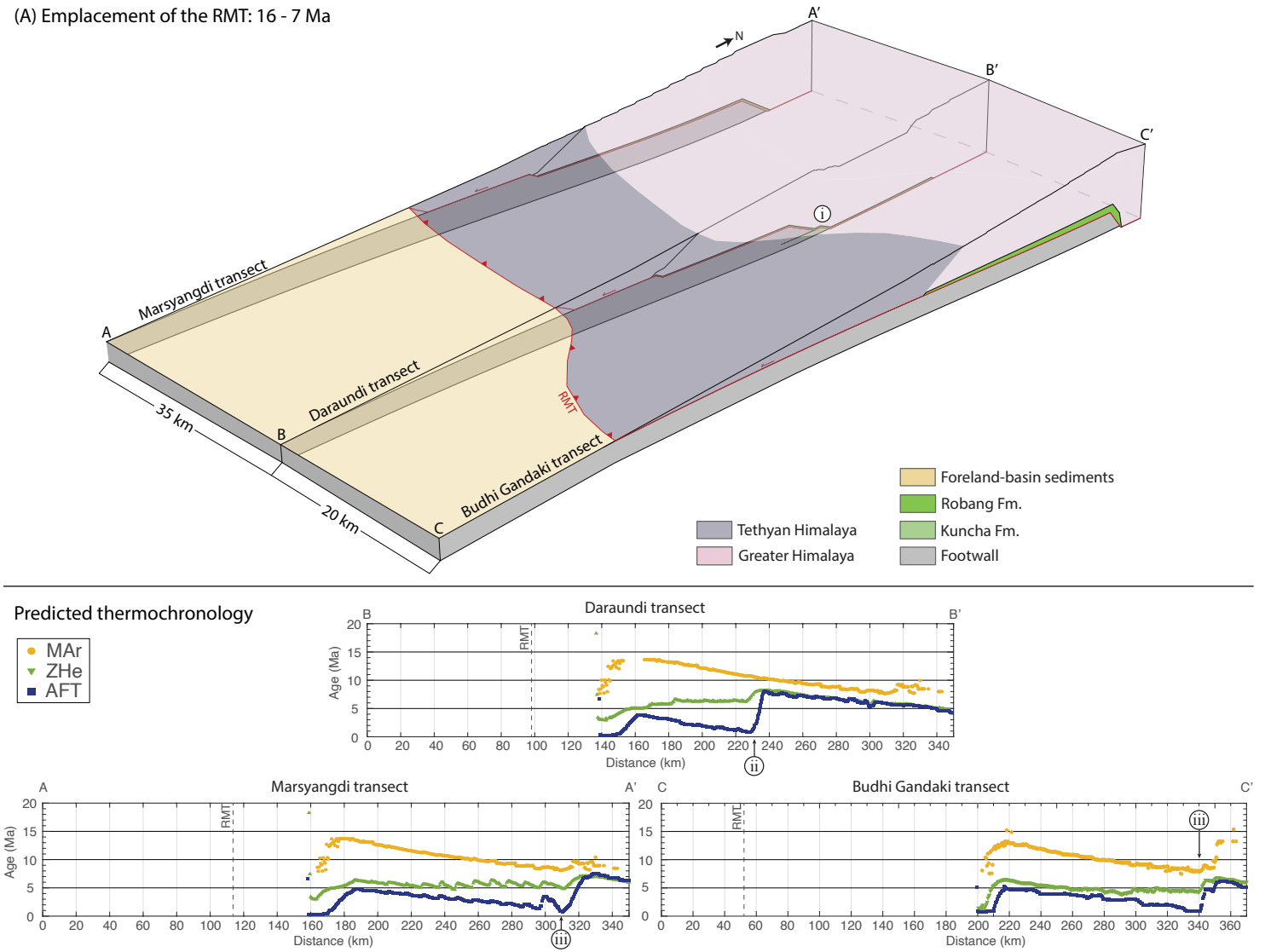

Figure 5. Evolution of the central Nepal Himalaya through time, showing predicted cooling ages for each transect (A-A′—Marsyangdi; B-B′—Daraundi; C-C′—Budhi Gandaki). Dating methods: MAr—muscovite Ar-Ar; ZHe—zircon (U-Th)/He; AFT—apatite fission track. Budhi Gandaki transect is shown at a greater relative distance from the Daraundi than in Figure 1 for clarity. The predicted cooling ages are plotted with respect to their distance from where the Main Frontal thrust surfaces. (A) Emplacement of the Ramgarh-Munsiari thrust (RMT): ca. 16–7 Ma. (*Continued on following 4 pages.*)

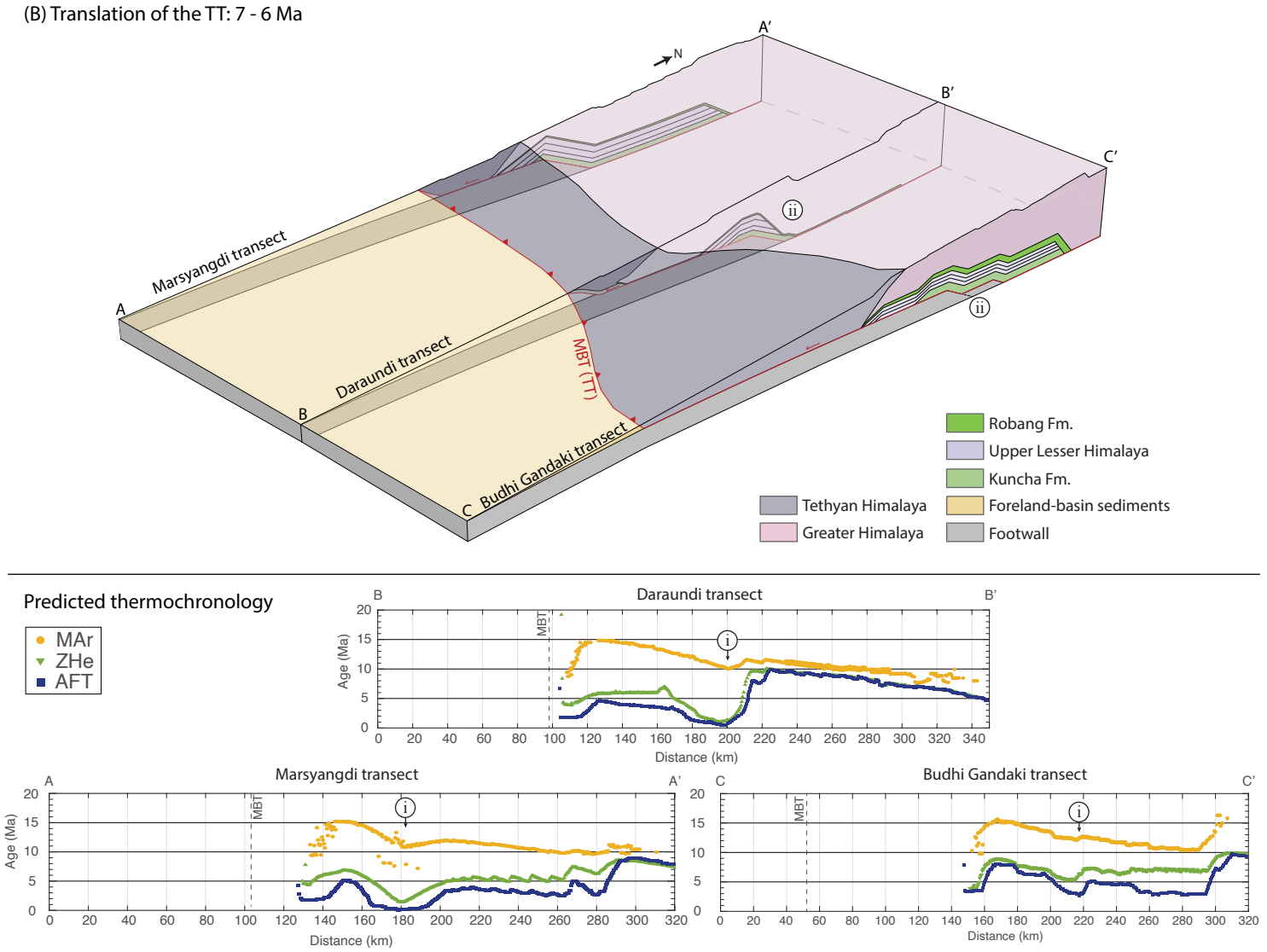

Figure 5 (*continued*). (B) Initiation and emplacement of the Trishuli thrust (TT): ca. 7–6 Ma. MBT—Main Boundary thrust. (*Continued on following 3 pages.*)

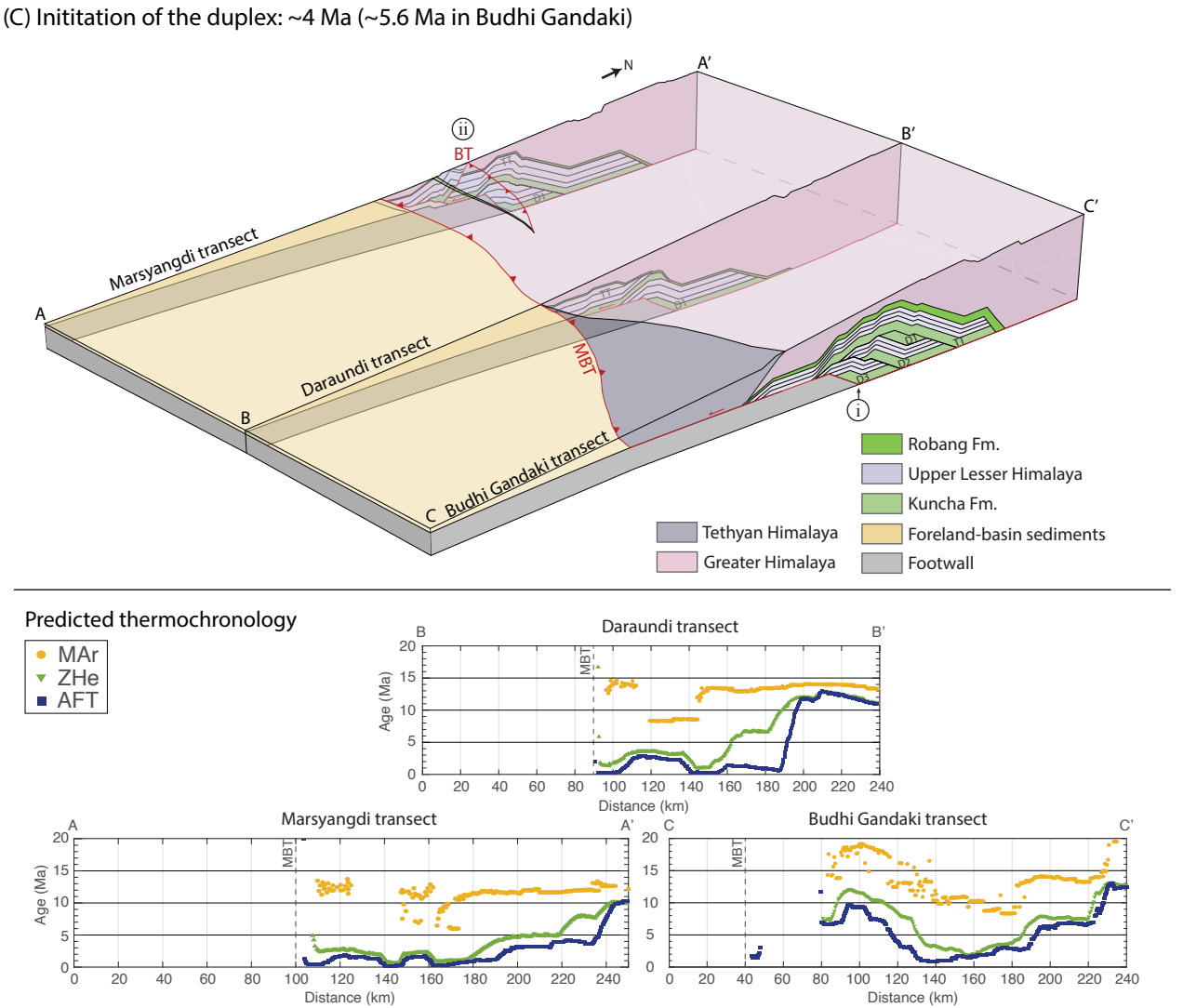

Figure 5 (*continued*). (C) Initiation of the duplex: ca. 4 Ma; in Budhi Gandaki transect: ca. 5.6 Ma. D1–D3 are the individual horses of the Lesser Himalayan duplex in the order that they deform. BT—backthrust present in the Marsyangdi transect. (*Continued on following 2 pages.*)

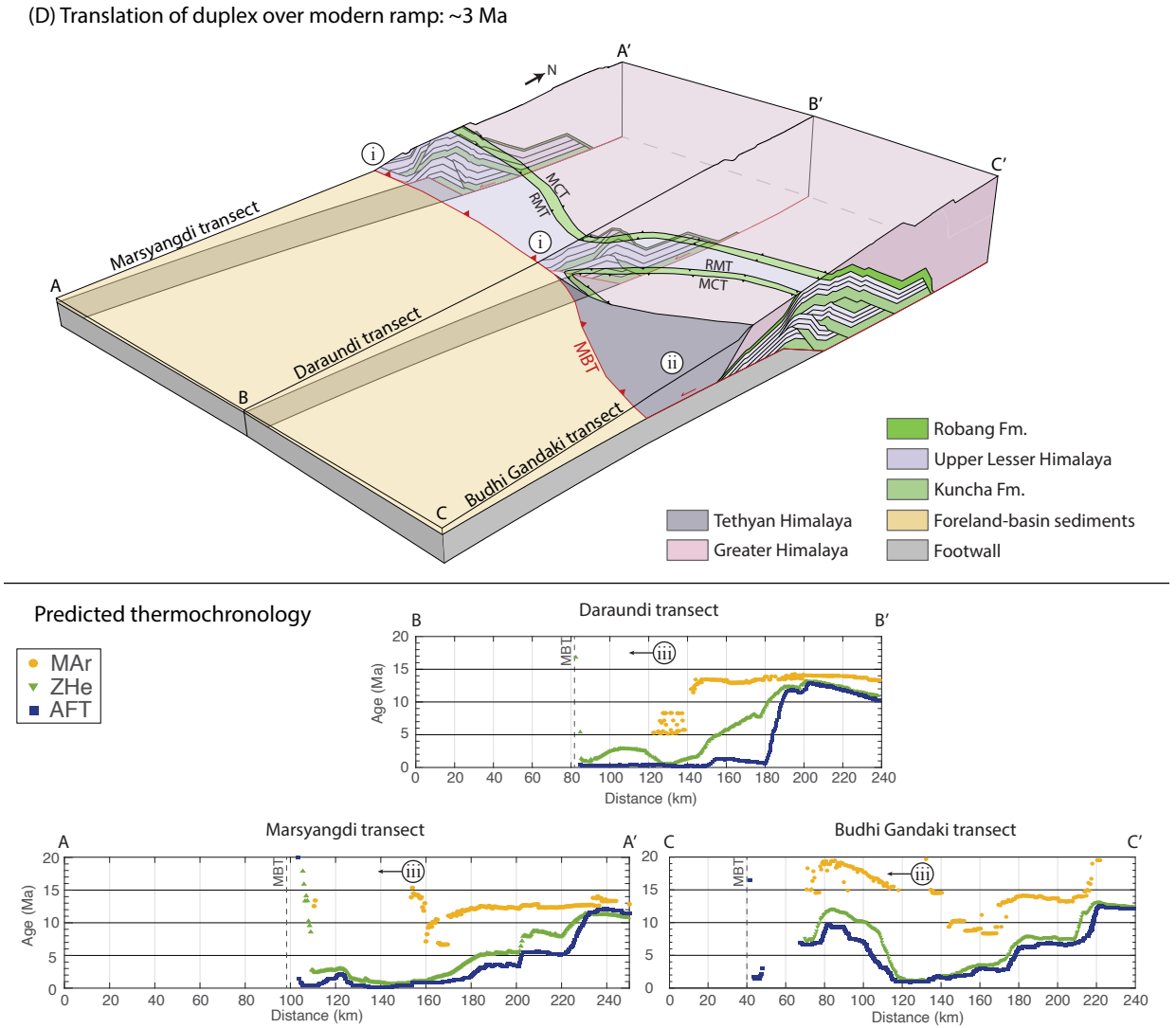

Figure 5 (*continued*). (D) Completion of duplex construction: ca. 3.2 Ma. MCT—Main Central thrust. (*Continued on following page.*)

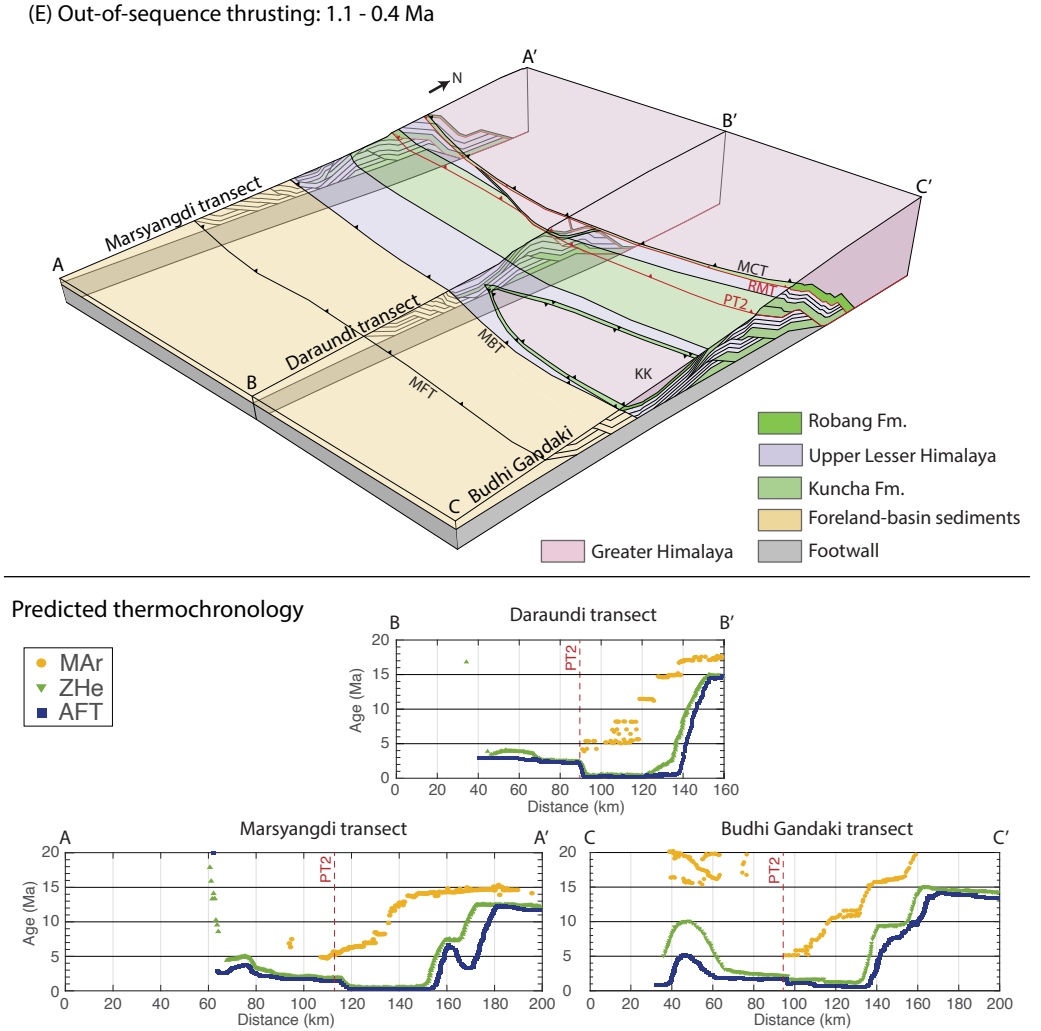

Figure 5 (*continued*). (E) Out-of-sequence thrusting in the hinterland: ca. 1.1 Ma. MFT—Main Frontal thrust; PT2—physiographic transition 2; KK—Kathmandu Klippe. Markers i, ii, and iii are discussed in text for each time slice.

(Fig. 4C; Fig. 5D, ii). The erosional removal of Greater Himalayan rocks over the duplex and the resulting exhumation of the underlying TT sheet creates a zone of unreset MAr ages. In the Daraundi and Marsyangdi transects, this unreset zone is largely continuous toward the south due to the lack of Greater Himalayan rocks exposed south of the duplex. However, the isolated klippe of Greater Himalayan rocks in the southern Budhi Gandaki transect show reset MAr ages that record the age of the emplacement of the RMT (Fig. 4C; Fig. 5D, iii). Following the translation of the duplex over the modern ramp via slip on the intra-Siwalik thrust sheets, hinterland OOS faulting initiates between 1.1 and 0.8 Ma with the reactivation of the RMT (Fig. 5E).

In the Marsyangdi and Budhi Gandaki transects, the alignment of the northern edge of the translated duplex and active ramp impart an advantageous northward dip to the weak and contiguous RMT fault plane. In the Daraundi transect, the surface trace of the RMT is located ~25 km farther to the south and the RMT exhibits a ramp-and-flat shape at the time of OOS faulting. We suggest that the length (~42 km) of the deeper, steeply dipping portion of the RMT in the Daraundi and its alignment with the contiguous RMT OOS fault in the Marsyangdi and Budhi Gandaki facilitated repetition of the Robang Formation and Greater Himalayan rocks in the Daraundi due to reactivation of the RMT. When the RMT is reactivated, the combination of the cross-sectional extent of the RMT from where it surfaces to where it meets the MHT between 135 and 170 km from the MFT (depending on the cross section; Fig. 4) and the final motion over the ramp due to the most recent activity at the MFT results in uplift and erosional exhumation occurring over this entire region, resetting AFT ages as far north as 165 km along the Marsyangdi transect (Fig. 4A). The northward limit of the associated young (ca. 1 Ma) reset Zhe ages is the base of the active ramp (Figs. 6–8).

Following the reactivation of the RMT in the Marsyangdi and Budhi Gandaki transects, OOS faulting steps southward and is accommodated on pre-existing fault zones that connect the active MHT ramp to the surface between 80 and 100 km from the MFT. Uplift along this OOS thrust creates the topographic transition zone known as physiographic transition 2 (PT2) (Wobus et al., 2003, 2006; Hodges et al., 2004; Whipple et al., 2016). In the Daraundi transect, the trace of PT2 is co-located with the surface trace of the original RMT (~86 km from the MFT). However, the complexity of the required path that the shortening would have to travel means that reactivation of the original RMT is unlikely (Fig. 4B). We suggest instead that the alignment of the footwall ramp of the TT in the Daraundi with the path of the OOS thrust in the Marsyangdi and Budhi Gandaki transects allowed the fault to seek out a more direct route to the surface (Fig. 5E). Motion on this new fault breaks the first horse of the duplex into two parts, offsetting the northern segment, and exhuming an ~30-km-wide region to the north of the trace of PT2. This additional exhumation results in a swath of reset AFT ages (ca. 0.5 Ma) extending 50 km from PT2 (~86 km) to the bottom of the MHT ramp (~136 km), along with reset ZHe ages (ca. 0.5–1 Ma) extending from PT2 to ~125 km from the MFT (Fig. 5E; Video S1, step 46). The cumulative effect of the motion on the RMT and PT2 is also visible in the Marsyangdi and Budhi Gandaki transects, with motion on PT2 resulting in reset AFT ages between the surface trace of PT2 and the bottom of the ramp (Fig. 5E; Videos S2 and S3). Finally, motion steps southwards again into the Siwalik Group, with motion on the intra-Siwalik thrust faults bringing the duplex over the active ramp into its final position.

6.2 Drivers of Along-Strike Changes of Upper Plate Geometry

Thermokinematic modeling of the Daraundi transect reveals how lateral changes in the upper plate that are visible today at the surface began as critical changes to the geometry of the MHT in the mid- to late Miocene. The most pronounced geometric change between the three sections is in the length of the TT sheet and the southern location of its trailing footwall. Along the Daraundi transect, the TT sheet is only 35 km long, compared to 120 km and 105 km in the Marsyangdi and Budhi Gandaki transects, respectively (Fig. 5A). Mostly due to this shorter length, the footwall ramp that facilitates the emplacement of the RMT over the rocks that make up the TT sheet along the Daraundi transect is ~100–110 km farther to the south than in the other transects. The northern edge of the TT sheet and the transition to the Robang Formation marks the distal edge of the Kuncha Formation (Pearson and DeCelles, 2005; Martin et al., 2011; Khanal and Robinson, 2013; Robinson and Pearson, 2013) and potentially the northern limit of the upper Lesser Himalaya. If so, the southern limit of the RMT footwall ramp would be a function of the geometry of the northern Indian margin, and this abrupt lateral step in the Indian margin (between the RMT footwall ramp in the Budhi Gandaki and Daraundi sections) may be related to features ascribed to the Judi lineament (Mugnier et al., 2011).

While the TT sheet is significantly shorter in the Daraundi transect than in the neighboring transects, the total amount of shortening that it accommodates (90 km) remains comparable to that in the neighboring Marsyangdi and Budhi Gandaki transects. This magnitude of shortening combined with its significantly shorter length means that the thrust sheet has been translated entirely over, and is currently south of, the modern ramp. Immediately prior to the initiation of the duplex in our model, the trailing end of the TT sheet is ~50 km farther to the south in the Daraundi compared to adjacent sections and is located over the first horse in the duplex (Fig. 5C; Video S1). In contrast, the first horse in the duplex initiates in the middle or near the southern, leading edge of the TT sheet in the neighboring Budhi Gandaki and Marsyangdi transects, respectively (Figs. 5C and 5D). Because of its limited length, magnitude of displacement, and southern location, motion on the TT also places a flat portion of the RMT and overlying Greater Himalayan rocks directly on top of the long northernmost horse of the duplex (Fig. 5C). This flat portion of the RMT and MCT directly over a flat portion of the Lesser Himalaya rocks in the duplex (Fig. 5D) is maintained following translation of the duplex over the modern ramp (Figs. 4 and 5E). The combination of a short TT sheet, comparatively high displacement, and the long length of the northernmost horse of the duplex produces the southern step in the trace of the RMT and MCT in the Daraundi compared to the neighboring two transects (Fig. 5E).

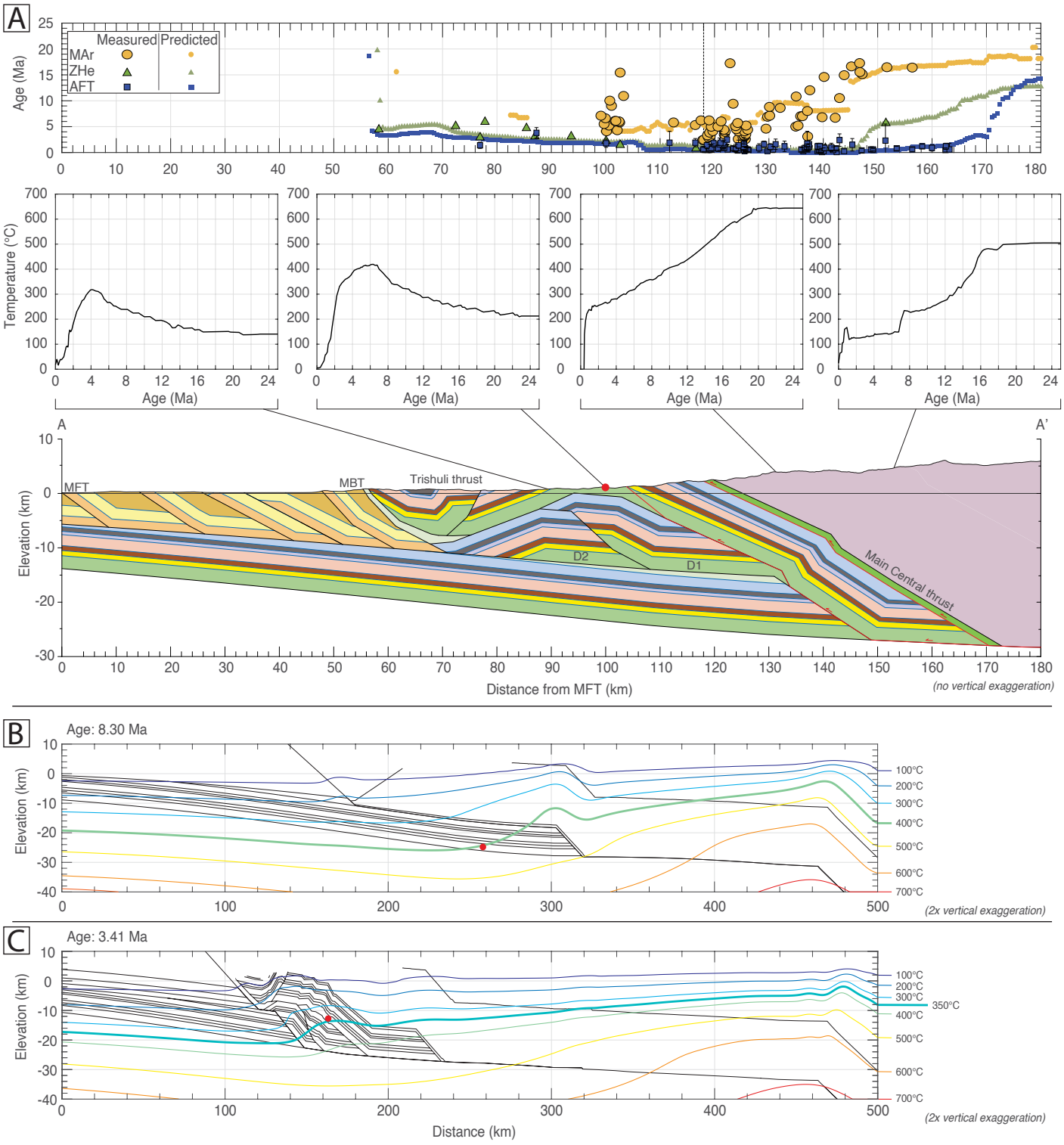

Figure 6. Thermal evolution of the Marsyangdi transect. (A) Comparisons of the time-temperature paths of representative parts of the cross section and the resulting predicted cooling ages. Dashed black line represents the location of the Main Central thrust. MFT—Main Frontal thrust; MBT—Main Boundary thrust; D1, D2—Horses of the Lesser Himalayan duplex in the order of their formation. Out-of-sequence faults are shown as red lines. Dating methods: MAr—muscovite Ar-Ar; ZHe—zircon (U-Th)/He; AFT—apatite fission track ± 2σ errors. (B) Isothermal plot showing the thermal field developed at 8.3 Ma, highlighting the heating above 400 °C. (C) Isothermal plot showing the thermal field developed at 3.4 Ma, highlighting the cooling below 350 °C. Black lines show the evolving structure of the transect. Red circle shows the thermokinematic evolution of rocks presently exposed 100 km from the MFT. All distances are measured with respect to the MFT.

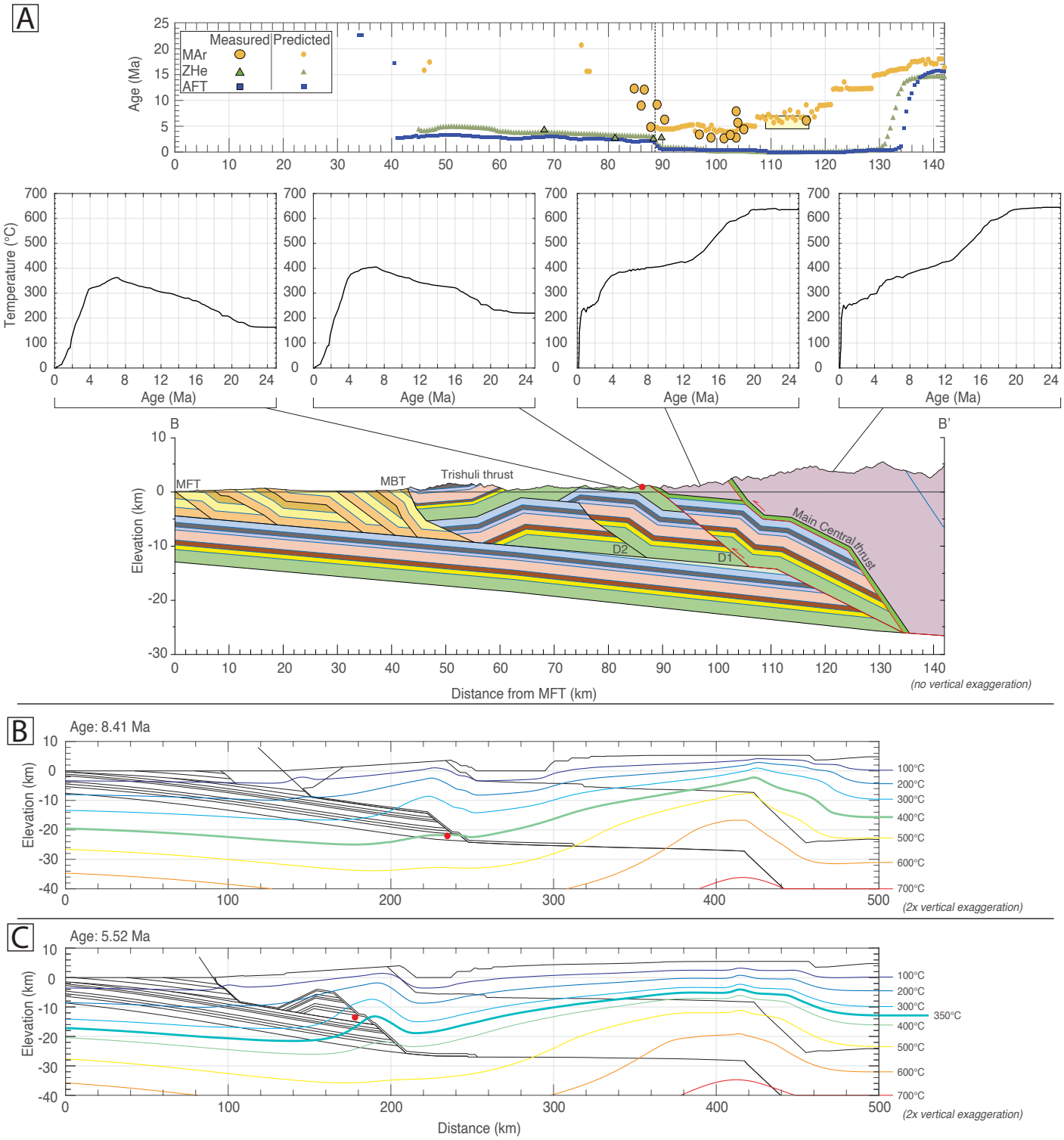

Figure 7. Thermal evolution of the Daraundi transect. (A) Comparisons of the time-temperature paths of representative parts of the cross section and the resulting predicted cooling ages. Dashed black line represents the location of the Main Central thrust. MFT—Main Frontal thrust; MBT—Main Boundary thrust; D1, D2—Horses of the Lesser Himalayan duplex in the order of their formation. Out-of-sequence faults are shown as red lines. Dating methods: MAr—muscovite Ar-Ar; ZHe—zircon (U-Th)/He; AFT—apatite fission track ± 2σ errors. (B) Isothermal plot showing the thermal field developed at 8.4 Ma, highlighting the heating above 400 °C. (C) Isothermal plot showing the thermal field developed at 5.5 Ma, highlighting the cooling below 350 °C. Black lines show the evolving structure of the transect. Red circle shows the thermokinematic evolution of rocks presently exposed 100 km from the MFT. All distances are measured with respect to the MFT.

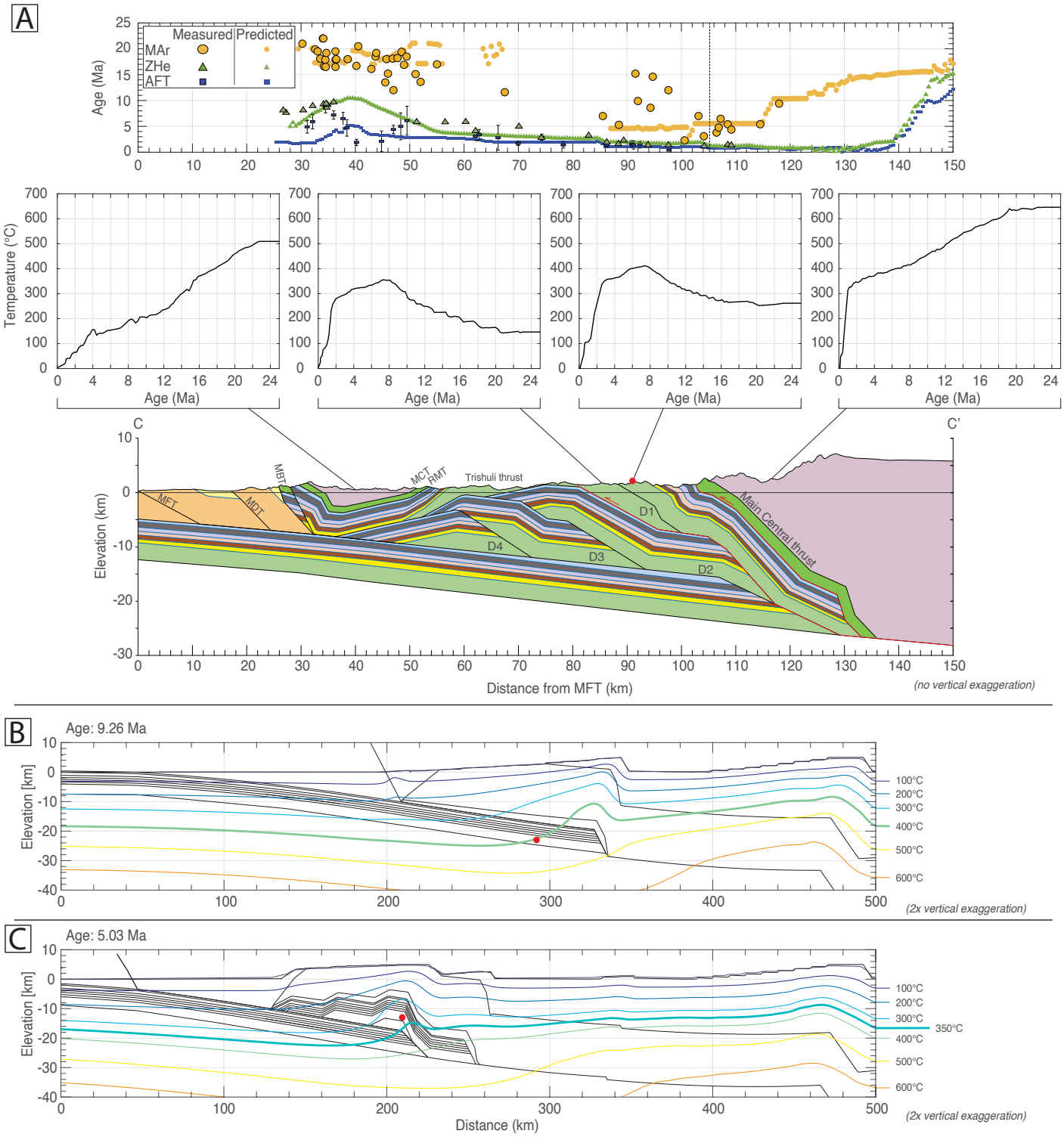

Figure 8. Thermal evolution of the Budhi Gandaki transect. (A) Comparisons of the time-temperature paths of representative parts of the cross section and the resulting predicted cooling ages. Dashed black line represents the location of the Main Central thrust (MCT). RMT—Ramgarh-Munsiari thrust; MBT—Main Boundary thrust; MDT—Main Dun thrust; MFT—Main Frontal thrust; D1, D2, D3, D4—Horses of the Lesser Himalayan duplex in the order of their formation. Out-of-sequence faults are shown as red lines. Dating methods: MAr—muscovite Ar-Ar; ZHe—zircon (U-Th)/He; AFT—apatite fission track ± 2σ errors. (B) Isothermal plot showing the thermal field developed at 9.3 Ma, highlighting the heating above 400 °C. (C) Isothermal plot showing the thermal field developed at 5 Ma, highlighting the cooling below 350 °C. Black lines show the evolving structure of the transect. Red circle shows the thermokinematic evolution of rocks presently exposed 90 km from the MFT. All distances are measured with respect to the MFT.

In addition to this southward step in the surface geology along the Daraundi transect, there is also a corresponding southward step in the distribution of young MAr ages (Fig. 2). While the active MHT ramp is located ~110 km from the MFT, the southernmost young MAr age is located 88 km from the MFT (Fig. 4B). In contrast to the southward step in the trace of the MCT and RMT unique to the Daraundi transect, the southward extent of young MAr ages continues west to the Marsyangdi (Fig. 2). Analyzing and comparing how key differences in the geometry of each transect has affected the resulting cooling histories highlights how this present-day distribution of reset MAr ages was formed. The southernmost of these reset MAr ages are located within the rocks of the Kuncha Formation, within the TT sheet along each transect. However, Kuncha samples from farther south on the TT have partially to fully unreset ages, requiring a difference in their cooling histories (Fig. 4). Examining the *t-T* histories of the TT sheet shows that the rocks along the northern edge of the TT subside and slowly warm due to adjacent emplacement of the MCT over the RMT (Figs. 6–8; Videos S1–S3; 23–16 Ma). The emplacement of the RMT over its footwall ramp (i.e., the trailing edge of the TT sheet) accelerates this heating by both increasing burial and advecting heat at the ramp. By the time that the RMT has been completely emplaced (8.4 Ma), the rocks that show reset ages have been heated to >400 °C (Figs. 6–8, red circle). Advection of heat at the ramp creates a pattern of southward-dipping isotherms, which place rocks located at the northern edge of the TT above the 400 °C isotherm while rocks located immediately to the south are never heated to above 370 °C (Figs. 6–8). Complete translation of the TT over its footwall ramp is required for the rocks to subsequently cool through below 350 °C, occurring at ca. 5.5 Ma along the Daraundi section, ca. 3.4 Ma along the Marsyangdi section, and ca. 5 Ma in the Budhi Gandaki section, setting the MAr ages (Figs. 6–8, red circles). Because TT rocks located immediately to the south were never heated above 370 °C, they were never fully reset and show partially to fully unreset ages. We find that the southern extent of reset MAr ages is controlled by the relationship between horses of the duplex that define the antiform, the resulting size of the duplex, and the modern MHT ramp. In the Marsyangdi, the horses of the duplex have been almost entirely translated over the ramp (Fig. 6). In the Daraundi, the horse that is part of the footwall ramp of PT2 has been entirely translated over the ramp. This allows rocks that have been heated above 400 °C to be exposed further south (Fig. 7). However, in the Budhi Gandaki, the longer N-S extent of the duplex means the northernmost horse (D2) has not been entirely translated over the MHT ramp, and the resulting TT overlying it is farther north (Fig. 8). This results in an offset in the distribution of cooling ages at the surface between the Budhi Gandaki and the Daraundi transects (Fig. 2).

6.3 Geometry of the Main Himalayan Thrust and Implications for Earthquake Rupture Extent

While mapping in central Nepal shows that the surface traces of the MCT and RMT and exposed Lesser Himalaya strata have significant along-strike variations in location and exposure along the northern limb of the Gorkha-Pokhara antiform, the geometry of the MHT and the recent OOS thrusts remain remarkably consistent between the Budhi Gandaki and Marsyangdi transects (Fig. 5E). The along-strike continuity of the MHT is seen in the distribution of the youngest reset ZHe and AFT ages (Figs. S1A and S1B), which are the most sensitive to the location of the active ramp (McQuarrie et al., 2019; Ghoshal et al., 2020, 2023; Robinson et al., 2021). This continuity is particularly notable in the linearity of the distribution of the ZHe ages (Fig. S1A). Unlike the measured MAr ages (Fig. 2), the youngest ZHe ages are located ~10 km to the north of the trace of the MCT in both the Marsyangdi and Budhi Gandaki transects and stay young at least 25 km north of the MCT (Fig. 4, Marsyangdi transect). Fault edges, step-overs, and changes in fault orientation and depth (fault ramps) have all been correlated with locations of rupture nucleation or termination and thus can exert a marked impact on rupture propagation and extent (King and Nábělek, 1985). This connection emphasizes the importance of documenting active fault geometry along seismogenic faults. Although the western edge of the Gorkha earthquake is aligned with an apparent seismic gap (Avouac, 2003), the MHT geometry is markedly uniform from the Trishuli valley in the east, to the Marsyangdi valley in the west (Figs. 1 and 4). Another property that may regulate earthquake nucleation is the potential dependency on temperature for creeping portions of megathrust faults (e.g., Marone, 1998; Hsu et al., 2009; Avouac et al., 2015). The transition between the locked and creeping portions of the MHT has been linked to a temperature of ~350 °C. Figure 9 shows the relationship between the underlying fault geometry and the modeled thermal field for each of the kinematic models explored here. Similar to Ghoshal et al. (2020), we find a strong spatial correlation between the 350 °C isotherm in the Daraundi and Budhi Gandaki transects with the locations of the Gorkha earthquake and the high-frequency seismic sources (Avouac et al., 2015) (Fig. 9), suggesting a thermo-rheological control on the nucleation and propagation of the earthquake. In contrast, in the Marsyangdi transect, the 350 °C isotherm is located on the mid-crustal ramp (Fig. 9A).

The strong spatial correlation between the earthquake epicenter and an inflection point in the path of the recently active PT2 OOS in the Daraundi transect is striking (Fig. 9B), with the inflection point representing an already weak point in the structure (e.g., King and Nábělek, 1985). The linearity of the modern MHT ramp and the OOS faults suggests a relationship between the two, particularly between the modern ramp and PT2 (e.g., Whipple et al., 2016). Along the Marsyangdi, the OOS fault at PT2 soles directly into the modern ramp, transferring motion on the ramp directly to the surface (Fig. 4A). Along the Daraundi, the OOS fault merges with the MHT <5 km south of the top of the ramp (Fig. 4B). During OOS fault displacement, the PT2 fault plane soled into the MHT at or immediately north of the mid-crustal ramp (Fig. 5). This relationship between the PT2 fault and the ramp would impart a linear geometry (and thus, a linear surface expression) to PT2 that has been used as a strong argument for its existence and recent activity (e.g., Wobus et al., 2003, 2006; Whipple et al., 2016). The co-location of the MHT-PT2 fault branch point and the 350 °C isotherm, particularly in the Daraundi (Gorkha) region (Figs. 1

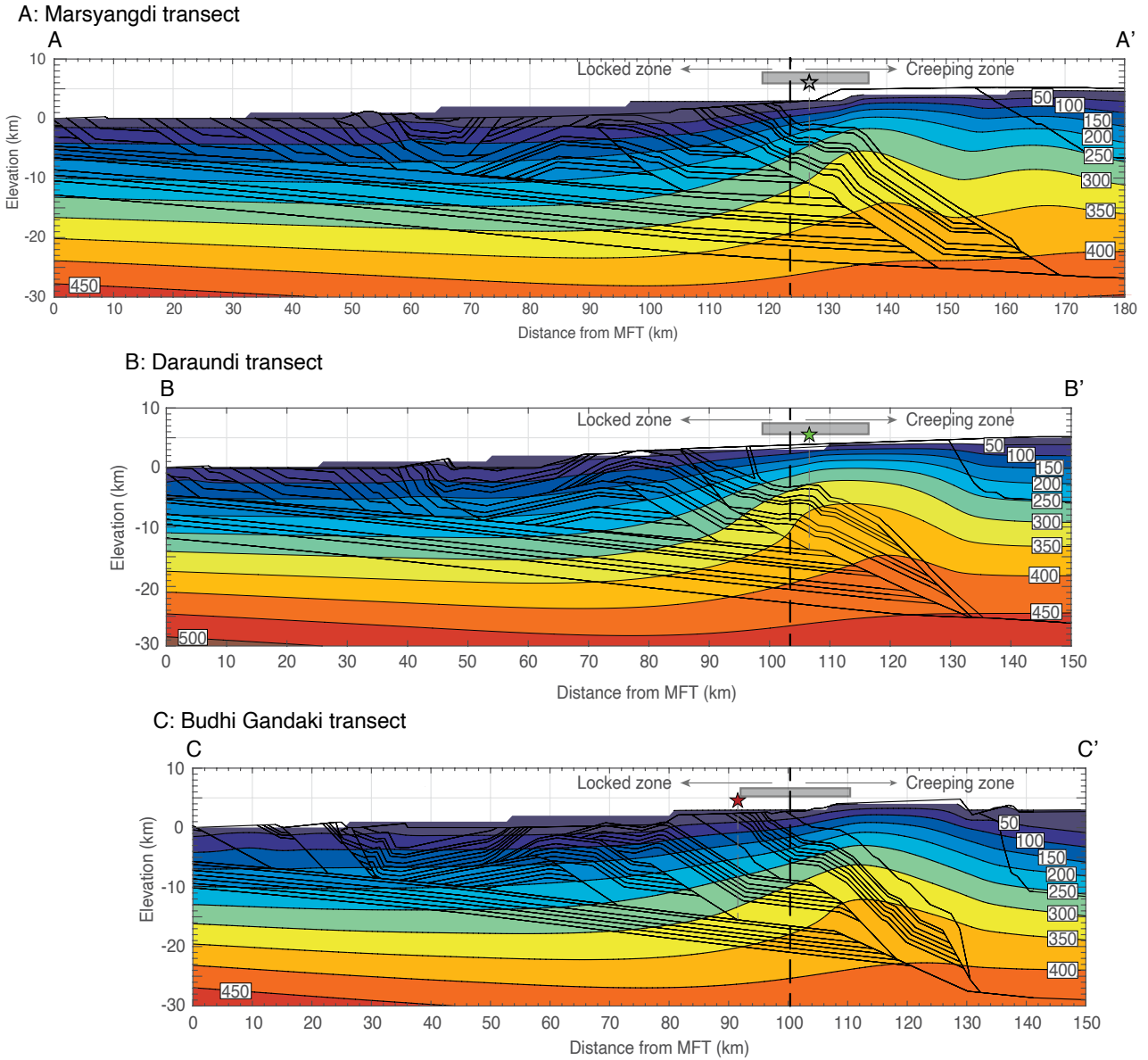

Figure 9. Comparison between the modeled thermal fields for each transect. (A) Marsyangdi, (B) Daraundi, (C) Budhi Gandaki. Transects are positioned with respect to the location of the Main Frontal thrust (MFT). Black lines show the final position of the deformed structures from the models. Green star is the epicenter of the 2015 Gorkha earthquake; red star, high-frequency seismic source in the Budhi Gandaki transect (Avouac et al., 2015); open black star, projected location of Gorkha epicenter on the Marsyangdi transect. Gray zone shows the spatial extent of high-frequency sources for the Gorkha earthquake (Grandin et al., 2015). Black dashed line shows the boundary between creeping and locked zones of the Main Himalayan thrust (Ader et al., 2012). Isotherms are labeled in °C.

and 9), is consistent with the OOS fault at PT2 absorbing a component of slip associated with the Gorkha earthquake (Whipple et al., 2016).

7. CONCLUSIONS

We combine detailed mapping and published MAr, zircon (U-Th)/He, and AFT ages with thermokinematic modeling to propose a new subsurface geometry and kinematic sequence for the Daraundi valley in central Nepal. Integrating this new geometry with previously proposed fault geometries for the neighboring Budhi Gandaki and Marsyangdi valleys allows us to develop an integrated kinematic evolution for central Nepal capable of modeling the distribution of cooling ages measured at the surface. We use this regional kinematic model to assess how the subsurface geometry of the region varies from east to west and evaluate the continuity of active structures over a distance of 100 km. While the southward step in the trace of the MCT and the coincident step in the distribution of reset MAr ages suggest that the geometry of the MHT changes between the Budhi Gandaki and Marsyangdi valleys, our modeling shows that these variations at the surface are caused by critical changes in the upper plate geometry. We show that the TT sheet is only ~35 km long in the Daraundi, compared to 105–120 km in the Budhi Gandaki and Marsyangdi, meaning that with similar magnitudes of displacement (~90–100 km) the footwall of the TT is translated 80–100 km farther to the south. The combination of this amount of displacement and short length of the Trishuli with the long northern horse of the Lesser Himalayan duplex results in the formation of the southward step in the surface geology. In addition, we find that the corresponding step in the reset MAr ages is controlled by the relationship between the modern MHT ramp and the geometry of the Lesser Himalayan duplex. Finally, a total of 10–15 km of OOS thrusting occurs across central Nepal, with the shortening split between two discrete fault zones that were aligned with the modern MHT ramp when they were active. The OOS faults and the active MHT ramp show a distinct linearity across central Nepal. The OOS motion is not the most recent component of deformation, estimated to have occurred between ca. 1.1 Ma and 0.2 Ma.

While the Daraundi valley is a zone of pronounced lateral variations in surface geology and measured MAr ages, these changes are not the result of variations in the geometry of the modern MHT, rather resulting from a change in the geometry of the rocks being translated over the ramp. As a result, we find no evidence for a significant lateral boundary in the MHT in the region that may have restricted the propagation of the 2015 Gorkha earthquake. Rather, we find that the nucleation of the earthquake is aligned with the 350 °C isotherm and the branch point between the MHT and an out-of-sequence thrust (PT2), while its westward propagation may have been restricted by the cooler rocks of the Marsyangdi transect.

ACKNOWLEDGMENTS

We would like to thank Willi Kappler (University of Tübingen) for his support in modifying the PECUBE-D software and cluster computing. We also thank the editors and two reviewers for their insightful comments and suggestions. This work was supported by an Andrew Mellon Predoctoral Fellowship from the University of Pittsburgh to SG, National Science Foundation Grants EAR-1524277 and EAR-1524320 to NM and DR, respectively, and a European Research Council Consolidator grant (615703) to TAE.

REFERENCES CITED

Ader, T., et al., 2012, Convergence rate across the Nepal Himalaya and interseismic coupling on the Main Himalayan Thrust: Implications for seismic hazard: Journal of Geophysical Research: Solid Earth, v. 117, B04403, https://doi.org/10.1029/2011JB009071.

Avouac, J.-P., 2003, Mountain building, erosion, and the seismic cycle in the Nepal Himalaya: Advances in Geophysics, v. 46, p. 1–80, https://doi.org/10.1016/S0065-2687(03)46001-9.

Avouac, J.-P., Meng, L., Wei, S., Wang, T., and Ampuero, J.-P., 2015, Lower edge of locked Main Himalayan Thrust unzipped by the 2015 Gorkha earthquake: Nature Geoscience, v. 8, p. 708–711, https://doi.org/10.1038/ngeo2518.

Bettinelli, P., Avouac, J.-P., Flouzat, M., Jouanne, F., Bollinger, L., Willis, P., and Chitrakar, G.R., 2006, Plate motion of India and interseismic strain in the Nepal Himalaya from GPS and DORIS measurements: Journal of Geodesy, v. 80, p. 567–589, https://doi.org/10.1007/s00190-006-0030-3.

Bilham, R., Larson, K., and Freymueller, J., 1997, GPS measurements of present-day convergence across the Nepal Himalaya: Nature, v. 386, p. 61–64, https://doi.org/10.1038/386061a0.

Brady, R.J., Ducea, M.N., Kidder, S.B., and Saleeby, J.B., 2006, The distribution of radiogenic heat production as a function of depth in the Sierra Nevada Batholith, California: Lithos, v. 86, p. 229–244, https://doi.org/10.1016/j.lithos.2005.06.003.

Braun, J., 2003, Pecube: A new finite-element code to solve the 3D heat transport equation including the effects of a time-varying, finite amplitude surface topography: Computers & Geosciences, v. 29, p. 787–794, https://doi.org/10.1016/S0098-3004(03)00052-9.

Braza, M., and McQuarrie, N., 2022, Determining the tempo of exhumation in the eastern Himalaya: Part 1. Geometry, kinematics and predicted cooling ages: Basin Research, v. 34, p. 141–169, https://doi.org/10.1111/bre.12615.

Braza, M., McQuarrie, N., Robinson, D.M., and Webb, L.E., 2023, Temperature, deformation, and mass transfer in a hot orogen: Insights from thermokinematic forward models for far western Nepal: Tectonics, v. 42, https://doi.org/10.1029/2023TC007912.

Brewer, I.D., Burbank, D.W., and Hodges, K.V., 2006, Downstream development of a detrital cooling-age signal: Insights from $^{40}Ar/^{39}Ar$ muscovite thermochronology in the Nepalese Himalaya, *in* Willett et al., eds., Tectonics, Climate, and Landscape Evolution: Geological Society of America Special Paper 398, p. 321–338, https://doi.org/10.1130/2006.2398(20).

Brookfield, M.E., 1993, The Himalayan passive margin from Precambrian to Cretaceous times: Sedimentary Geology, v. 84, p. 1–35, https://doi.org/10.1016/0037-0738(93)90042-4.

Burbank, D.W., Beck, R.A., and Mulder, T., 1996, The Himalayan foreland basin, *in* Yin, A., and Harrison, T.M., eds., The Tectonic Evolution of Asia: Cambridge, UK, Cambridge University Press, p. 149–188.

Catlos, E.J., Harrison, T.M., Kohn, M.J., Grove, M., Ryerson, F.J., Manning, C.E., and Upreti, B.N., 2001, Geochronologic and thermobarometric constraints on the evolution of the Main Central Thrust, central Nepal Himalaya: Journal of Geophysical Research: Solid Earth, v. 106, p. 16,177–16,204, https://doi.org/10.1029/2000JB900375.

Catlos, E.J., Lovera, O.M., Kelly, E.D., Ashley, K.T., Harrison, T.M., and Etzel, T., 2018, Modeling high-resolution pressure-temperature paths across the Himalayan Main Central Thrust (central Nepal): Implications for the dynamics of collision: Tectonics, v. 37, p. 2363–2388, https://doi.org/10.1029/2018TC005144.

Colchen, M., Le Fort, P., and Pêcher, A., 1986, Recherches géologiques dans l'Himalaya du Nepal: Annapurna, Manaslu, Ganesh Himal—Notice de la carte géologique au 1/200 000e: Paris, Centre National de la Recherche Scientifique, 137 p.

Coleman, M.E., 1996, The tectonic evolution of the central Himalaya, Marsyandi Valley, Nepal [Ph.D. thesis]: Cambridge, Massachusetts Institute of Technology, 221 p.

Corrie, S.L., and Kohn, M.J., 2011, Metamorphic history of the central Himalaya, Annapurna region, Nepal, and implications for tectonic models: Geological Society of America Bulletin, v. 123, p. 1863–1879, https://doi.org/10.1130/B30376.1.

Cross, E.A., III, 2014, The structure, stratigraphy, and evolution of the Lesser Himalaya of central Nepal [M.S. thesis]: Tucson, University of Arizona, 83 p.

DeCelles, P.G., Gehrels, G.E., Quade, J., and Ojha, T.P., 1998, Eocene-early Miocene foreland basin development and the history of Himalayan thrusting, western and central Nepal: Tectonics, v. 17, p. 741–765, https://doi.org/10.1029/98TC02598.

DeCelles, P.G., Gehrels, G.E., Quade, J., LaReau, B., and Spurlin, M., 2000, Tectonic implications of U-Pb zircon ages of the Himalayan orogenic belt in Nepal: Science, v. 288, p. 497–499, https://doi.org/10.1126/science.288.5465.497.

DeCelles, P.G., Quade, J., Kapp, P., Fan, M., Dettman, D.L., and Ding, L., 2007, High and dry in central Tibet during the Late Oligocene: Earth and Planetary Science Letters, v. 253, p. 389–401, https://doi.org/10.1016/j.epsl.2006.11.001.

Dhital, M.R., 2015, Geology of the Nepal Himalaya: Regional Perspective of the Classic Collided Orogen: Cham, Switzerland, Springer International Publishing, 498 p., https://doi.org/10.1007/978-3-319-02496-7.

Dodson, M.H., 1973, Closure temperature in cooling geochronological and petrological systems: Contributions to Mineralogy and Petrology, v. 40, p. 259–274, https://doi.org/10.1007/BF00373790.

Ehlers, T.A., 2023, Pecube-D: Thermokinematic and erosion modeling software for problems in tectonics and surface processes: https://doi.org/10.5281/zenodo.7785668 (last accessed August 2023).

Ehlers, T.A., et al., 2005, Computational tools for low-temperature thermochronometer interpretation: Reviews in Mineralogy and Geochemistry, v. 58, p. 589–622, https://doi.org/10.2138/rmg.2005.58.22.

Elliott, J.R., Jolivet, R., González, P.J., Avouac, J.-P., Hollingsworth, J., Searle, M.P., and Stevens, V.L., 2016, Himalayan megathrust geometry and relation to topography revealed by the Gorkha earthquake: Nature Geoscience, v. 9, p. 174–180, https://doi.org/10.1038/ngeo2623.

England, P., Le Fort, P., Molnar, P., and Pêcher, A., 1992, Heat sources for Tertiary metamorphism and anatexis in the Annapurna-Manaslu Region, central Nepal: Journal of Geophysical Research: Solid Earth, v. 97, p. 2107–2128, https://doi.org/10.1029/91JB02272.

Gansser, A., 1964, Geology of the Himalayas: New York, Wiley-Interscience, 289 p.

Gautam, P., and Rösler, W., 1999, Depositional chronology and fabric of Siwalik Group sediments in central Nepal from magnetostratigraphy and magnetic anisotropy: Journal of Asian Earth Sciences, v. 17, p. 659–682, https://doi.org/10.1016/S1367-9120(99)00021-8.

Gehrels, G.E., Blakey, R., Karlstrom, K.E., Timmons, J.M., Dickinson, B., and Pecha, M., 2011, Detrital zircon U-Pb geochronology of Paleozoic strata in the Grand Canyon, Arizona: Lithosphere, v. 3, p. 183–200, https://doi.org/10.1130/L121.1.

Ghoshal, S., McQuarrie, N., Robinson, D.M., Adhikari, D.P., Morgan, L.E., and Ehlers, T.A., 2020, Constraining central Himalayan (Nepal) fault geometry through integrated thermochronology and thermokinematic modeling: Tectonics, v. 39, https://doi.org/10.1029/2020TC006399.

Ghoshal, S., McQuarrie, N., Huntington, K.W., Robinson, D.M., and Ehlers, T.A., 2023, Testing erosional and kinematic drivers of exhumation in the central Himalaya: Earth and Planetary Science Letters, v. 609, https://doi.org/10.1016/j.epsl.2023.118087.

Gilmore, M.E., McQuarrie, N., Eizenhöfer, P.R., and Ehlers, T.A., 2018, Testing the effects of topography, geometry, and kinematics on modeled thermochronometer cooling ages in the eastern Bhutan Himalaya: Solid Earth, v. 9, p. 599–627, https://doi.org/10.5194/se-9-599-2018.

Grandin, R., Vallée, M., Satriano, C., Lacassin, R., Klinger, Y., Simoes, M., and Bollinger, L., 2015, Rupture process of the M_w = 7.9 2015 Gorkha earthquake (Nepal): Insights into Himalayan megathrust segmentation: Geophysical Research Letters, v. 42, p. 8373–8382, https://doi.org/10.1002/2015GL066044.

Hames, W.E., and Bowring, S.A., 1994, An empirical evaluation of the argon diffusion geometry in muscovite: Earth and Planetary Science Letters, v. 124, p. 161–169, https://doi.org/10.1016/0012-821X(94)00079-4.

Harrison, T.M., Copeland, P., Hall, S.A., Quade, J., Burner, S., Ojha, T.P., and Kidd, W.S.F., 1993, Isotopic preservation of Himalayan/Tibetan uplift, denudation, and climatic histories of two molasse deposits: The Journal of Geology, v. 101, p. 157–175, https://doi.org/10.1086/648214.

Harrison, T.M., Ryerson, F.J., Le Fort, P., Yin, A., Lovera, O.M., and Catlos, E.J., 1997, A Late Miocene-Pliocene origin for the Central Himalayan inverted metamorphism: Earth and Planetary Science Letters, v. 146, p. E1–E7, https://doi.org/10.1016/S0012-821X(96)00215-4.

Hodges, K.V., 2014, Thermochronology in orogenic systems, *in* Rudnick, R.L., ed., Treatise on Geochemistry (second edition), Volume 4: The Crust: Amsterdam, Elsevier, p. 281–308, https://doi.org/10.1016/B978-0-08-095975-7.00308-9.

Hodges, K.V., Wobus, C., Ruhl, K., Schildgen, T., and Whipple, K., 2004, Quaternary deformation, river steepening, and heavy precipitation at the front of the Higher Himalayan ranges: Earth and Planetary Science Letters, v. 220, p. 379–389, https://doi.org/10.1016/S0012-821X(04)00063-9.

Hourigan, J.K., Reiners, P.W., and Brandon, M.T., 2005, U-Th zonation-dependent alpha-ejection in (U-Th)/He chronometry: Geochimica et Cosmochimica Acta, v. 69, p. 3349–3365, https://doi.org/10.1016/j.gca.2005.01.024.

Hsu, Y.-J., Avouac, J.-P., Yu, S.-B., Chang, C.-H., Wu, Y.-M., and Woessner, J., 2009, Spatio-temporal slip, and stress level on the faults within the western foothills of Taiwan: Implications for fault frictional properties: Pure and Applied Geophysics, v. 166, p. 1853–1884, https://doi.org/10.1007/s00024-009-0510-5.

Hubbard, J., Almeida, R., Foster, A., Sapkota, S.N., Bürgi, P., and Tapponnier, P., 2016, Structural segmentation controlled the 2015 M_w 7.8 Gorkha earthquake rupture in Nepal: Geology, v. 44, p. 639–642, https://doi.org/10.1130/G38077.1.

Huntington, K.W., Blythe, A.E., and Hodges, K.V., 2006, Climate change and Late Pliocene acceleration of erosion in the Himalaya: Earth and Planetary Science Letters, v. 252, p. 107–118, https://doi.org/10.1016/j.epsl.2006.09.031.

Huntington, K.W., Ehlers, T.A., Hodges, K.V., and Whipp, D.M., 2007, Topography, exhumation pathway, age uncertainties, and the interpretation of thermochronometer data: Tectonics, v. 26, TC4012, https://doi.org/10.1029/2007TC002108.

Jouanne, F., Mugnier, J.L., Gamond, J.F., Fort, P.L., Pandey, M.R., Bollinger, L., Flouzat, M., and Avouac, J.P., 2004, Current shortening across the Himalayas of Nepal: Geophysical Journal International, v. 157, p. 1–14, https://doi.org/10.1111/j.1365-246X.2004.02180.x.

Kayal, J.R., 2008, Microearthquake Seismology and Seismotectonics of South Asia: Dordrecht, Springer, 503 p., https://doi.org/10.1007/978-1-4020-8180-4.

Ketcham, R.A., 1996, Distribution of heat-producing elements in the upper and middle crust of southern and west central Arizona: Evidence from the core complexes: Journal of Geophysical Research: Solid Earth, v. 101, p. 13,611–13,632, https://doi.org/10.1029/96JB00664.

Ketcham, R.A., Carter, A., Donelick, R.A., Barbarand, J., and Hurford, A.J., 2007, Improved modeling of fission-track annealing in apatite: American Mineralogist, v. 92, p. 799–810, https://doi.org/10.2138/am.2007.2281.

Khanal, S., 2014, Structural and kinematic evolution of the Himalayan thrust belt, central Nepal [Ph.D. thesis]: Tuscaloosa, University of Alabama, 202 p.

Khanal, S., and Robinson, D.M., 2013, Upper crustal shortening and forward modeling of the Himalayan thrust belt along the Budhi-Gandaki River, central Nepal: International Journal of Earth Sciences, v. 102, p. 1871–1891, https://doi.org/10.1007/s00531-013-0889-1.

Kimura, K., 1999, Diachronous evolution of sub-Himalayan piggyback basins, Nepal: Island Arc, v. 8, p. 99–113, https://doi.org/10.1046/j.1440-1738.1999.00224.x.

King, G., and Nábělek, J., 1985, Role of fault bends in the initiation and termination of earthquake rupture: Science, v. 228, p. 984–987, https://doi.org/10.1126/science.228.4702.984.

Kohn, M.J., 2008, P-T-t data from central Nepal support critical taper and repudiate large-scale channel flow of the Greater Himalayan Sequence: Geological Society of America Bulletin, v. 120, p. 259–273, https://doi.org/10.1130/B26252.1.

Kohn, M.J., Catlos, E.J., Ryerson, F.J., and Harrison, T.M., 2001, Pressure-temperature-time path discontinuity in the Main Central thrust zone, central Nepal: Geology, v. 29, p. 571–574, https://doi.org/10.1130/0091-7613(2001)029<0571:PTTPDI>2.0.CO;2.

Kohn, M.J., Wieland, M.S., Parkinson, C.D., and Upreti, B.N., 2004, Miocene faulting at plate tectonic velocity in the Himalaya of central Nepal: Earth and Planetary Science Letters, v. 228, p. 299–310, https://doi.org/10.1016/j.epsl.2004.10.007.

Kuiper, K.F., Deino, A., Hilgen, F.J., Krijgsman, W., Renne, P.R., and Wijbrans, J.R., 2008, Synchronizing rock clocks of Earth history: Science, v. 320, p. 500–504, https://doi.org/10.1126/science.1154339.

Larson, K.P., Godin, L., and Price, R.A., 2010, Relationships between displacement and distortion in orogens: Linking the Himalayan foreland and hinterland in central Nepal: Geological Society of America Bulletin, v. 122, p. 1116–1134, https://doi.org/10.1130/B30073.1.

Lavé, J., and Avouac, J.P., 2000, Active folding of fluvial terraces across the Siwaliks Hills, Himalayas of central Nepal: Journal of Geophysical Research: Solid Earth, v. 105, p. 5735–5770, https://doi.org/10.1029/1999JB900292.

Lavé, J., and Avouac, J.P., 2001, Fluvial incision and tectonic uplift across the Himalayas of central Nepal: Journal of Geophysical Research: Solid Earth, v. 106, p. 26,561–26,591, https://doi.org/10.1029/2001JB000359.

Lock, J., and Willett, S., 2008, Low-temperature thermochronometric ages in fold-and-thrust belts: Tectonophysics, v. 456, p. 147–162, https://doi.org/10.1016/j.tecto.2008.03.007.

Marone, C., 1998, Laboratory-derived friction laws and their application to seismic faulting: Annual Review of Earth and Planetary Sciences, v. 26, p. 643–696, https://doi.org/10.1146/annurev.earth.26.1.643.

Martin, A.J., DeCelles, P.G., Gehrels, G.E., Patchett, P.J., and Isachsen, C., 2005, Isotopic and structural constraints on the location of the Main Central thrust in the Annapurna Range, central Nepal Himalaya: Geological Society of America Bulletin, v. 117, p. 926–944, https://doi.org/10.1130/B25646.1.

Martin, A.J., Burgy, K.D., Kaufman, A.J., and Gehrels, G.E., 2011, Stratigraphic and tectonic implications of field and isotopic constraints on depositional ages of Proterozoic Lesser Himalayan rocks in central Nepal: Precambrian Research, v. 185, p. 1–17, https://doi.org/10.1016/j.precamres.2010.11.003.

McQuarrie, N., and Ehlers, T.A., 2015, Influence of thrust belt geometry and shortening rate on thermochronometer cooling ages: Insights from thermokinematic and erosion modeling of the Bhutan Himalaya: Tectonics, v. 34, p. 1055–1079, https://doi.org/10.1002/2014TC003783.

McQuarrie, N., and Ehlers, T.A., 2017, Techniques for understanding fold-and-thrust belt kinematics and thermal evolution, *in* Law, R.D., Thigpen, J.R., Merschat, A.J., and Stowell, H.H., eds., Linkages and Feedbacks in Orogenic Systems: Geological Society of America Memoir 213, p. 25–54, https://doi.org/10.1130/2017.1213(02).

McQuarrie, N., Eizenhöfer, P.R., Long, S.P., Tobgay, T., Ehlers, T.A., Blythe, A.E., Morgan, L.E., Gilmore, M.E., and Dering, G.M., 2019, The influence of foreland structures on hinterland cooling: Evaluating the drivers of exhumation in the eastern Bhutan Himalaya: Tectonics, v. 38, p. 3282–3310, https://doi.org/10.1029/2018TC005340.

Menon, R., Kumar, P.S., Reddy, G.K., and Srinivasan, R., 2003, Radiogenic heat production of Late Archaean Bundelkhand granite and some Proterozoic gneisses and granitoids of central India: Current Science, v. 85, p. 634–638.

Mugnier, J.L., Huyghe, P., Gajurel, A.P., Upreti, B.N., and Jouanne, F., 2011, Seismites in the Kathmandu basin and seismic hazard in central Himalaya: Tectonophysics, v. 509, p. 33–49, https://doi.org/10.1016/j.tecto.2011.05.012.

Mugnier, J.-L., Gajurel, A., Huyghe, P., Jayangondaperumal, R., Jouanne, F., and Upreti, B., 2013, Structural interpretation of the great earthquakes of the last millennium in the central Himalaya: Earth-Science Reviews, v. 127, p. 30–47, https://doi.org/10.1016/j.earscirev.2013.09.003.

Mugnier, J.-L., Jouanne, F., Bhattarai, R., Cortes-Aranda, J., Gajurel, A., Leturmy, P., Robert, X., Upreti, B., and Vassallo, R., 2017, Segmentation of the Himalayan megathrust around the Gorkha earthquake (25 April 2015) in Nepal: Journal of Asian Earth Sciences, v. 141, p. 236–252, https://doi.org/10.1016/j.jseaes.2017.01.015.

Ojha, T.P., Butler, R.F., Quade, J., DeCelles, P.G., Richards, D., and Upreti, B.N., 2000, Magnetic polarity stratigraphy of the Neogene Siwalik Group at Khutia Khola, far western Nepal: Geological Society of America Bulletin, v. 112, p. 424–434, https://doi.org/10.1130/0016-7606(2000)112<424:MPSOTN>2.0.CO;2.

Ojha, T.P., Butler, R.F., DeCelles, P.G., and Quade, J., 2009, Magnetic polarity stratigraphy of the Neogene foreland basin deposits of Nepal: Basin Research, v. 21, p. 61–90, https://doi.org/10.1111/j.1365-2117.2008.00374.x.

Olree, E.C., 2018, Kinematic and flexural isostasy modeling in central Nepal: Using erosional, depositional, and cooling histories to validate a balanced cross section [M.S. thesis]: Tuscaloosa, University of Alabama, 88 p.

Pandey, M.R., Tandukar, R.P., Avouac, J.P., Lavé, J., and Massot, J.P., 1995, Interseismic strain accumulation on the Himalayan crustal ramp (Nepal): Geophysical Research Letters, v. 22, p. 751–754, https://doi.org/10.1029/94GL02971.

Parsons, A.J., Law, R.D., Searle, M.P., Phillips, R.J., and Lloyd, G.E., 2016, Geology of the Dhaulagiri-Annapurna-Manaslu Himalaya, Western Region, Nepal. 1:200,000: Journal of Maps, v. 12, p. 100–110, https://doi.org/10.1080/17445647.2014.984784.

Pearson, O.N., 2002, Structural evolution of the central Nepal fold-thrust belt and regional tectonic and structural significance of the Ramgarh thrust [Ph.D. thesis]: Tucson, University of Arizona, 231 p.

Pearson, O.N., and DeCelles, P.G., 2005, Structural geology and regional tectonic significance of the Ramgarh thrust, Himalayan fold-thrust belt of Nepal: Tectonics, v. 24, TC4008, https://doi.org/10.1029/2003TC001617.

Qiu, Q., Hill, E.M., Barbot, S., Hubbard, J., Feng, W., Lindsey, E.O., Feng, L., Dai, K., Samsonov, S.V., and Tapponnier, P., 2016, The mechanism of partial rupture of a locked megathrust: The role of fault morphology: Geology, v. 44, p. 875–878, https://doi.org/10.1130/G38178.1.

Quade, J., Cater, J.M.L., Ojha, T.P., Adam, J., and Harrison, T.M., 1995, Late Miocene environmental change in Nepal and the northern Indian subcontinent: Stable isotopic evidence from paleosols: Geological Society of America Bulletin, v. 107, p. 1381–1397, https://doi.org/10.1130/0016-7606(1995)107<1381:LMECIN>2.3.CO;2.

Rahn, M.K., and Grasemann, B., 1999, Fission track and numerical thermal modeling of differential exhumation of the Glarus thrust plane (Switzerland): Earth and Planetary Science Letters, v. 169, p. 245–259, https://doi.org/10.1016/S0012-821X(99)00078-3.

Ratschbacher, L., Frisch, W., Liu, G., and Chen, C., 1994, Distributed deformation in southern and western Tibet during and after the India-Asia collision: Journal of Geophysical Research: Solid Earth, v. 99, p. 19,917–19,945, https://doi.org/10.1029/94JB00932.

Ray, L., Bhattacharya, A., and Roy, S., 2007, Thermal conductivity of Higher Himalayan Crystallines from Garhwal Himalaya, India: Tectonophysics, v. 434, p. 71–79, https://doi.org/10.1016/j.tecto.2007.02.003.

Reiners, P.W., 2005, Zircon (U-Th)/He thermochronometry: Reviews in Mineralogy and Geochemistry, v. 58, p. 151–179, https://doi.org/10.2138/rmg.2005.58.6.

Reiners, P.W., Spell, T.L., Nicolescu, S., and Zanetti, K.A., 2004, Zircon (U-Th)/He thermochronometry: He diffusion and comparisons with $^{40}Ar/^{39}Ar$ dating: Geochimica et Cosmochimica Acta, v. 68, p. 1857–1887, https://doi.org/10.1016/j.gca.2003.10.021.

Renne, P.R., Knight, K.B., Nomade, S., Leung, K.-N., and Lou, T.-P., 2005, Application of deuteron-deuteron (D-D) fusion neutrons to $^{40}Ar/^{39}Ar$ geochronology: Applied Radiation and Isotopes, v. 62, p. 25–32, https://doi.org/10.1016/j.apradiso.2004.06.004.

Robert, X., van der Beek, P., Braun, J., Perry, C., and Mugnier, J.-L., 2011, Control of detachment geometry on lateral variations in exhumation rates in the Himalaya: Insights from low-temperature thermochronology and numerical modeling: Journal of Geophysical Research: Solid Earth, v. 116, B05202, https://doi.org/10.1029/2010JB007893.

Robinson, D.M., and Martin, A.J., 2014, Reconstructing the Greater Indian margin: A balanced cross section in central Nepal focusing on the Lesser Himalayan duplex: Tectonics, v. 33, p. 2143–2168, https://doi.org/10.1002/2014TC003564.

Robinson, D.M., and Pearson, O.N., 2013, Was Himalayan normal faulting triggered by initiation of the Ramgarh-Munsiari thrust and development of the Lesser Himalayan duplex?: International Journal of Earth Sciences, v. 102, p. 1773–1790, https://doi.org/10.1007/s00531-013-0895-3.

Robinson, D.M., Khanal, S., Olree, E., Bhattacharya, G., and Mandal, S., 2021, Controls of stratigraphic architecture on along strike cooling age patterns: Terra Nova, v. 33, p. 129–136, https://doi.org/10.1111/ter.12498.

Ruppel, C., and Hodges, K.V., 1994, Role of horizontal thermal conduction and finite time thrust emplacement in simulation of pressure-temperature-time paths: Earth and Planetary Science Letters, v. 123, p. 49–60, https://doi.org/10.1016/0012-821X(94)90256-9.

Sakai, H., 1983, Geology of the Tansen Group of the Lesser Himalaya in Nepal: Memoirs of the Faculty of Science, Kyushu University, Series D, Geology, v. XXV, p. 27–74, https://doi.org/10.5109/1546083.

Sakai, H., 1985, Rifting of the Gondwanaland and uplifting of the Himalayas recorded in Mesozoic and Tertiary fluvial sediments in the Nepal Himalayas, *in* Taira, A., and Masuda, F., eds., Sedimentary Facies in the Active Plate Margin: Tokyo, Terra Scientific Publishing, p. 723–732.

Sastri, V.V., Bhandari, L.L., Raju, A.T.R., and Datta, A.K., 1971, Tectonic framework and subsurface stratigraphy of the Ganga basin: Journal of the Geological Society of India, v. 12, p. 222–233.

Schmitz, M.D., and Bowring, S.A., 2001, U-Pb zircon and titanite systematics of the Fish Canyon Tuff: An assessment of high-precision U-Pb geochronology and its application to young volcanic rocks: Geochimica et Cosmochimica Acta, v. 65, p. 2571–2587, https://doi.org/10.1016/S0016-7037(01)00616-0.

Scholz, C.H., 1998, Earthquakes and friction laws: Nature, v. 391, p. 37–42, https://doi.org/10.1038/34097.

Shi, Y., and Wang, C.-Y., 1987, Two-dimensional modeling of the *P-T-t* paths of regional metamorphism in simple overthrust terrains: Geology, v. 15, p. 1048–1051, https://doi.org/10.1130/0091-7613(1987)15<1048:TMOTPP>2.0.CO;2.

Stevens, V.L., and Avouac, J.P., 2015, Interseismic coupling on the main Himalayan thrust: Geophysical Research Letters, v. 42, p. 5828–5837, https://doi.org/10.1002/2015GL064845.

Tokuoka, T., Takayasu, K., Yoshida, M., and Hisatomi, K., 1986, The Churia (Siwalik) Group of the Arung Khola area, west central Nepal: Memoirs of the Faculty of Science, Shimane University, v. 20, p. 135–210.

Upreti, B.N., 1996, Stratigraphy of the western Nepal Lesser Himalaya: A synthesis: Journal of Nepal Geological Society, v. 13, p. 11–28, https://doi.org/10.3126/jngs.v13i0.32127.

USGS (U.S. Geological Survey), 2015, M 7.8—67 km NNE of Bharatpur, Nepal: https://earthquake.usgs.gov/earthquakes/eventpage/us20002926/executive (last accessed 11 May 2015).

Whipp, D.M., Ehlers, T.A., Blythe, A.E., Huntington, K.W., Hodges, K.V., and Burbank, D.W., 2007, Plio-Quaternary exhumation history of the central Nepalese Himalaya: 2. Thermokinematic and thermochronometer age prediction model: Tectonics, v. 26, TC3003, https://doi.org/10.1029/2006TC001991.

Whipple, K.X., Shirzaei, M., Hodges, K.V., and Arrowsmith, J.R., 2016, Active shortening within the Himalayan orogenic wedge implied by the 2015 Gorkha earthquake: Nature Geoscience, v. 9, p. 711–716, https://doi.org/10.1038/ngeo2797.

Wobus, C.W., Hodges, K.V., and Whipple, K.X., 2003, Has focused denudation sustained active thrusting at the Himalayan topographic front?: Geology, v. 31, p. 861–864, https://doi.org/10.1130/G19730.1.

Wobus, C.W., Whipple, K.X., and Hodges, K.V., 2006, Neotectonics of the central Nepalese Himalaya: Constraints from geomorphology, detrital $^{40}Ar/^{39}Ar$ thermochronology, and thermal modeling: Tectonics, v. 25, TC4011, https://doi.org/10.1029/2005TC001935.

Yagi, Y., and Okuwaki, R., 2015, Integrated seismic source model of the 2015 Gorkha, Nepal, earthquake: Geophysical Research Letters, v. 42, p. 6229–6235, https://doi.org/10.1002/2015GL064995.

Zhang, J., and Guo, L., 2007, Structure and geochronology of the southern Xainza-Dinggye rift and its relationship to the south Tibetan detachment system: Journal of Asian Earth Sciences, v. 29, p. 722–736, https://doi.org/10.1016/j.jseaes.2006.05.003.